International Communications in Heat and Mass Transfer 169 (2025) 109506

Contents lists available at ScienceDirect

International Communications in Heat and Mass Transfer

journal homepage: www.elsevier.com/locate/ichmt

Thermal efficiency evaluation using hybrid ANN-CFD simulations of natural convective flow in rectangular open-ended cavities filled with nanoencapsulated PCM

Mohammad Abbaszadeh [a,*], Alireza Timas [b], Mojtaba Mirzaei [a], Iman Hosseini [a], Mohammad Ghalambaz [c,d]

[a] Hydro-Aeronautical Research Center, Shiraz University, Shiraz, Iran
[b] School of Mechanical Engineering, Shiraz University, Shiraz, Iran
[c] Department of Mathematical Sciences, Saveetha School of Engineering, SIMATS, Chennai, India
[d] Laboratory on Convective Heat and Mass Transfer, Tomsk State University, 634050 Tomsk, Russia

ARTICLE INFO

Keywords:
Open-ended cavity
Hybrid CFD-ANN modeling
Artificial Neural Network (ANN)
Nano-Encapsulated Phase Change Material (NEPCM)
Natural convection
Entropy generation

ABSTRACT

This study comprehensively investigates natural convection within open cavities filled with nano-encapsulated phase change materials (NEPCM), emphasizing the effects of aspect ratio, Rayleigh number, Stefan number, and NEPCM concentration on thermal performance. A rigorously validated two-dimensional computational fluid dynamics (CFD) model was employed to accurately analyze the complex thermofluidic behavior, with resulting data subsequently utilized to train an artificial neural network (ANN) for rapid and precise performance prediction. The findings demonstrate that the use of NEPCM significantly enhances heat transfer, with the average Nusselt number increasing by up to 2.19 times at a Rayleigh number of $Ra = 10^4$ and an aspect ratio of $A_s = 0.1$. This enhancement diminishes with increasing aspect ratio, reflecting a complex relationship between geometric configuration and thermal performance. Additionally, higher Stefan numbers positively influence heat transfer dynamics. The ANN model exhibits exceptional predictive accuracy ($R^2 > 0.999$), enabling rapid parametric analysis and optimization. The hybrid CFD-ANN approach thus serves as a robust and practical tool for the design and optimization of thermal management systems, applicable in passive cooling, latent heat storage, and electronic cooling applications.

1. Introduction

Among the forefront topics in contemporary engineering research, natural convection in open and closed cavities has emerged as a significant and widely applied topic in engineering research, attracting considerable attention from scholars due to its extensive applications in various industries. These include solar heating systems [1], the automotive sector [2], power generation units [3], and many other domains. With the advancement of science and technology, the use of phase change materials (PCMs) has become increasingly feasible, especially in systems constrained by physical size, chemical sensitivity, or specific operational requirements. PCMs are capable of absorbing and releasing substantial amounts of latent heat energy within compact volumes, without undergoing chemical reactions or incurring notable thermal losses. Consequently, they are particularly valuable in cooling systems [4], heat exchangers [5,6], and power generation applications, such as nuclear and solar power plants [7–10].

Nevertheless, the primary limitation of PCMs remains their poor thermal conductivity, which significantly hampers efficient heat transfer [11]. Hence, the charging and discharging processes of latent heat thermal energy storage (LHTES) systems are typically slow and time-consuming due to the inherently low thermal conductivity of PCMs. This limitation poses a significant challenge in applications where rapid thermal response is crucial. Consequently, extensive efforts have been made to enhance the thermal performance of these systems. In particular, researchers have investigated various strategies to improve heat transfer rates, including the use of nano-additives [12], extended surfaces like fins [13,14], or helical surfaces [15], metal foams [16], and advanced encapsulation technologies [17,18].

Despite the significant industrial relevance of natural convection and PCMs, natural convection in open cavities remains a persistent and challenging problem. This complexity arises from intricate fluid flow and heat transfer mechanisms induced by temperature gradients and

* Corresponding author.
E-mail address: Mabbaszadeh@shirazu.ac.ir (M. Abbaszadeh).

https://doi.org/10.1016/j.icheatmasstransfer.2025.109506

Nomenclature

Acronyms

NEPCM	Nano-Encapsulated Phase Change Material	ANN	Artificial Neural Network

Greek Symbols

ϕ	Volume fraction of NEPCM particles	ρ	Density, (kg/m^3)
μ	Dynamic viscosity, (kg/ms)	β	Thermal expansion coefficient, (1/K)
α	Thermal diffusivity, (m^2/s)	θ_f	Non-dimensional fusion temperature
κ	Thermal conductivity, (W/mK)	η	Thermal efficiency parameter
$\dot{S}'''_{gen}$	Entropy generation per unit volume, $(W/(m^3K))$		

Roman Symbols

u, v	Velocities in x and y directions, (m/s)	p	Pressure, (Pa)
T	Temperature, (K)	T_h, T_c	Hot wall and opening temperatures
C_p	Specific heat capacity, (J/(kg K))	k	Thermal conductivity, (W/(m K))
g	Gravitational acceleration, (m/s^2)	H	Height of cavity, (m)
h_{sf}	Latent heat of fusion, (J/kg)	T_f	Fusion temperature, (K)
T_{Mr}	Temperature interval of phase change, (K)	ΔT	Temperature difference, $(T_h - T_c)$
Nu	Local Nusselt number	Nu_{ave}	Average Nusselt number
S_g	Dimensionless entropy generation	S_{ave}	Average dimensionless entropy generation
Cr	Heat capacity ratio	Ste	Stefan number
Ra	Rayleigh number	Pr	Prandtl number

Subscripts

m	Mixture (suspension)	f	Base fluid (water)
p	Particle (NEPCM)	sh	Shell (polyurethane)
co	Core (nonadecane)	s	Simulated (CFD result)
a	Predicted (ANN result)	x, y	Spatial directions
0	Base case (pure fluid, no NEPCM)	amb	ambient

buoyancy forces. In open cavities, the absence of enclosed boundaries on one or more sides complicates flow behavior and makes its prediction challenging. This complexity increases further when internal elements such as baffles are introduced, as demonstrated by Rashid et al. [19]. A similar effect is observed when curved internal geometries, such as hemispherical obstacles, are introduced, which can significantly influence velocity profiles and pressure distributions within lid-driven cavities, [20]. Previous research has significantly enhanced our understanding of various aspects of free convection in open-ended cavities, particularly concerning important parameters such as Rayleigh number (Ra) [21], inclination [22], and aspect ratio (As) [23]. Furthermore, a comprehensive review of mixed convection in open cavity-channel systems has been conducted, highlighting the need to address persistent gaps such as the lack of experimental data and the limited exploration of flow enhancement techniques [24]. Additionally, the location of the heat source within the cavity has been shown to play a crucial role in the efficiency of mixed convection, as demonstrated by Rashid et al. [25]. In line with these investigations, Mohamad et al. [26] utilized the Lattice Boltzmann Method (LBM) to simulate natural convection in open-ended cavities. Their work highlighted the intricate physics of flow and heat transfer, providing insights into the effects of boundary conditions and the stability of the flow field. They demonstrated that the Nusselt number (Nu) is significantly influenced by the Ra and the As, establishing crucial correlations for predicting thermal performance in such cavities. Sanjari et al. [27] delved into the intricate dynamics of natural convection in an inclined open-ended cavity partially filled with fibrous porous media. They analyzed the effects of the porous media's properties and the cavity's inclination angle on heat transfer and fluid flow characteristics. Their findings underscore the critical role these parameters play in enhancing the thermal performance and efficiency of such systems. Ait Haj Said et al. [28] conducted a numerical investigation of free convection in an axisymmetric open-ended cavity heated from below. Their findings revealed that as the Ra and As increase, the heat transfer transitions from a predominantly conductive mode to a convective mode, thereby enhancing thermal performance. They also proposed useful correlations for the Nu, which are valuable for practical applications in thermal systems. Another important contribution was made by Chaabane et al. [29], who utilized the lattice Boltzmann method to simulate magneto-hydrodynamic free convection heat transfer in two-dimensional cavities, highlighting the impact of Rayleigh and Hartmann numbers on flow and temperature fields.

Another persistent challenge faced by researchers is the use of PCMs in open enclosures. In such systems, direct exposure to the environment and the possibility of heat loss result in reduced heat transfer rates and a non-uniform, slow melting process [17,30]. Moreover, the location of the enclosure's opening plays a crucial role in the development of natural convection currents. For instance, configurations with top openings can significantly intensify heat dissipation and lead to a considerable reduction in thermal energy storage efficiency [31]. Therefore, the encapsulation of PCMs is considered an effective approach for their integration into porous structures. This technique involves creating a protective shell around the PCM, which prevents leakage during phase transitions and consequently enhances the mechanical and chemical stability of the material over multiple thermal cycles [32]. Furthermore, by appropriately selecting the shell material, thermal conductivity can be improved, and issues such as nanoparticle agglomeration or sedimentation in composite systems can be mitigated [33,34]. These characteristics help maintain the latent heat capacity and thermodynamic stability of the PCM, which are crucial in numerous heat transfer applications, particularly in the thermal management of photovoltaic systems [35]. Nevertheless, although some researchers have pointed to limitations such as reduced thermal efficiency, gradual degradation over multiple cycles, and challenges related to cost-effective and practical encapsulation [36,37], numerous studies have effectively demonstrated the significant advantages of NEPCMs in various applications. As an example, a recent study by Hassan et al. [38] investigated the cooling performance of a central processing unit within a trapezoidal enclosure filled with NEPCM, under the influence of a rotating cylinder and a magnetic field. The results revealed that increasing the Reynolds and Richardson numbers enhanced heat and mass transfer by up to 80.5% and 147.9%, respectively. In contrast, an increase in the Hartmann number weakened convection, leading to reductions in the Nu and Sherwood numbers by up to 12.7% and 39.5%, respectively. The highest thermal efficiency was observed at a fusion temperature of 0.5.

To further improve the performance of NEPCM-based systems, attention has also been directed toward enhancing the thermophysical properties of the encapsulated material itself. In this context, Timuralp et al. [39] explored the nanoencapsulation of a phase change material (PCM) based on a capric-myristic acid mixture containing copper oxide (CuO) nanoparticles for thermal energy storage applications. In their study, urea-formaldehyde resin was employed as the shell material, aiming to enhance thermal properties and prevent leakage. The results demonstrated that the addition of CuO nanoparticles significantly improved the thermal stability and mechanical strength of the NEPCM, shifting the thermal decomposition temperature to the range of 22.78 °Celsius to 29.45 °Celsius. Considering the surrounding environmental conditions of the equipment, the presence of a magnetic field is also a natural occurrence. For this purpose, Hussain et al. [40] investigated the bio-convective flow of phase change encapsulated nanofluids (NEPCM) within a retro-prismatic enclosure subjected to an inclined magnetic field. An additional numerical investigation explored the effects of confined Lorentz forces on micropolar fluid dynamics in lid-driven cavities, as shown by Ahmad et al. [41]. Extending previous studies on natural convection heat transfer in NEPCM-based nanofluids, Sudarsana Reddy et al. [42] examined the natural heat transfer performance of such fluids inside a square cavity using the finite element method. Their findings revealed that increasing the NEPCM volume fraction from 1% to 5% enhanced the heat transfer rate by up to 42% compared to the base fluid. Additionally, an increase in the Stefan number (Ste) improved the dimensionless heat transfer characteristics. Sreedevi and Reddy [43] investigated heat and mass transfer, as well as the flow behavior of microorganisms in a porous cavity filled with NEPCM under the influence of a magnetic field. The results indicated that increasing the Ste reduces the melting time and enhances the control over the melting temperature of the NEPCM. Despite significant advancements in improving the thermal behavior of NEPCM-based systems through physical and material modifications, as highlighted in previous studies, there remains an increasing need for intelligent and adaptive approaches to accurately predict and optimize thermal performance under varying operational conditions while reducing the computational burden associated with repeated simulations [43,44].

Despite the efficiency of classical numerical methods, they are often computationally expensive and face limitations when dealing with high-dimensional parametric spaces or nonlinear interactions in complex geometries. In contrast, data-driven approaches particularly machine learning and Artificial Intelligence (AI) techniques, or more precisely, computer-based algorithms applied to various heat transfer problems have increasingly emerged as powerful alternatives in the field of thermal engineering. These algorithms offer the potential to accelerate design processes, enhance predictive accuracy, and even enable real-time control of thermal management systems [45,46]. The artificial intelligence algorithms employed in this domain serve as elementary representations of human intelligence and evolutionary knowledge [47]. Among the widely adopted approaches is the Artificial Neural Network (ANN), which has gained significant traction due to its versatility [48]. ANNs can be trained using both Supervised and Unsupervised experimental datasets [49], making them effective tools across a broad spectrum of heat transfer applications. These include solar energy systems, the design of steam-generating power plants, estimation of thermal loads in buildings, and the prediction of airflow in naturally ventilated test chambers [50]. One of the key advantages of using ANNs for simulating thermal processes is their ability to provide fast and reliable performance predictions once properly trained. For instance, Alotaibi et al. [51] investigated the heat transfer performance of NEPCM within a porous triangular enclosure equipped with a cold fin and a partially heated source, under the influence of a magnetic field. In this study, an ANN model with supervised learning was employed to predict the Nu. The dataset comprised 103 samples, which were randomly divided into three subsets: 70% for training, 15% for validation, and 15% for testing the model. As part of the literature review, the study conducted by Upreti et al. [52] can be highlighted, in which the three-dimensional magneto-hydrodynamic flow of a NEPCM over a wedge was analyzed, considering the effects of Hall current and ion slip. To solve the governing equations of flow and energy, physics-informed neural networks (PINNs), developed based on the architecture of ANNs, were employed. This method operates without relying on experimental data or conventional data splitting into training, validation, and testing sets, and is instead trained solely based on the governing differential equations.

Additionally, other recent studies have expanded the investigation of thermal behavior and flow characteristics of encapsulated phase change nanofluids (NEPCM) in complex geometries, using advanced numerical techniques and AI algorithms. Tayebi et al. [53] employed a multilayer perceptron (MLP) neural network model to analyze natural convection of non-Newtonian NEPCM within a non-Darcy porous cavity under local thermal non-equilibrium (LTNE) conditions. Their results indicated that although solid and fluid phases are sensitive to physical parameters, the suspended phase exhibits greater responsiveness to Ra and Darcy (Da) numbers. The accuracy of the ANN in predicting the Nu was confirmed with a high correlation coefficient. Further, Alsedias et al. [54] studied the effects of exothermic reactions and double-diffusive phenomena on the flow of non-Newtonian NEPCM in a curved channel containing internal ellipses. By integrating the incompressible smoothed particle hydrodynamics (ISPH) method with an ANN model, they demonstrated that increasing the power-law index (n) and the (Ra) significantly reduced the apparent viscosity and flow velocity, leading to improved thermal uniformity. Moreover, the ANN model showed high agreement with ISPH-derived data. In a related investigation, Hassan et al. [55] utilized an Arbitrary Lagrangian-Eulerian (ALE) approach alongside the finite element method to examine the combined effects of magnetic fields and boundary oscillations in a baffled U-shaped enclosure filled with NEPCM. Their findings revealed that increasing the Ra from 10^3 to 10^5 had the greatest impact on heat transfer enhancement, with the average Nu rising by up to 129.8%. Additionally, increasing nanoparticle concentration from 0.01 to 0.04 led to an improvement in heat transfer rate by 58.9%. Collectively, these studies demonstrate that the integration of AI-driven modeling and numerical simulation offers a powerful framework for accurately analyzing the thermal behavior of phase change nanofluids in complex geometries, potentially paving the way for optimized performance in energy thermal management systems.

Nevertheless, a noticeable research gap persists in the context of free convective flow in open cavities filled with NEPCMs. Despite the growing interest in utilizing NEPCMs to enhance heat transfer performance, studies specifically investigating their behavior in open geometries remain scarce. Open cavities offer unique advantages, such as ease of construction and potential applications in thermal energy storage systems. However, the geometric As of the cavity an important parameter influencing flow and heat transfer has not received adequate attention to date. Understanding how the As affects the thermal and flow behavior of NEPCMs in open cavities could provide novel insights and lead to optimized designs for practical implementations. Accordingly, this study explores these under-investigated areas to fully harness the potential of NEPCMs in free convective flow scenarios. In addition, to establish a benchmark framework for future research involving the application of ANNs and other modeling approaches in the specialized analysis of natural convection in open cavities containing NEPCMs, the current research employs ANN models to predict thermal performance η and average Nu with high accuracy. The remainder of this paper is structured to guide the reader through a logical progression of the study. Following the introduction, Section 2 presents the physical model, encompassing the geometrical configuration, governing equations, thermophysical properties of the NEPCM suspension, and the imposed boundary conditions. To ensure the reliability of the numerical framework, a mesh independence test is conducted, and the model is thoroughly validated against established benchmark results. Building

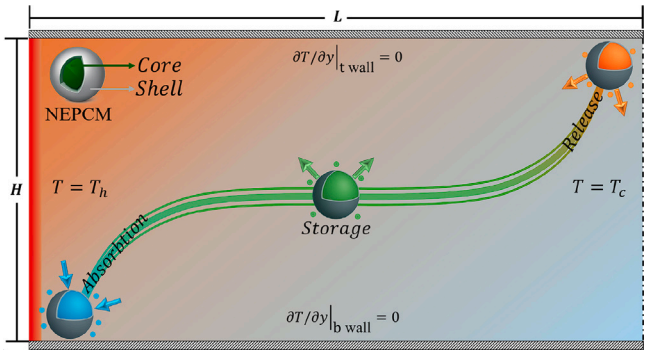

Fig. 1. Schematic diagram of geometry under consideration.

upon this foundation, Section 3 delves into a comprehensive parametric analysis, examining how key factors such as the As, Rayleigh number, Ste, and fusion temperature influence the thermal and thermodynamic behavior of the system. Subsequently, Section 3.1 introduces an ANN model developed to predict the average Nusselt number and thermal efficiency based on the simulation data, with its performance evaluated using standard statistical metrics. Finally, Section 4 concludes the paper by summarizing the main findings, highlighting their engineering significance, and outlining potential applications of NEPCMs in next-generation thermal energy storage technologies.

2. Mathematical analysis

2.1. Problem statement

In the present study, the investigated physical model consists of a 2D open cavity with an As ranging from 0.25 to 10. The cavity is filled with a mixture of water and NEPCM, and natural convection is induced within the domain. The configuration of the model is illustrated in Fig. 1. The cavity dimensions are defined by a characteristic length L and height H. A key feature of this model is the presence of an open surface that is in direct contact with the surrounding environment. Moreover, the encapsulated nanofluid inside the cavity undergoes three fundamental thermal processes energy absorption, storage, and release which are depicted by the curved line in Fig. 1. The left wall is uniformly heated to a high temperature T_h, while the right wall is maintained at a lower cold temperature T_c. The remaining two walls are thermally insulated. It should be noted that the system is a flow-through configuration, where the so-called cavity is part of a larger reservoir or tank. While it is open in the sense that it exchanges fluid with the larger system, the open connection to the large reservoir allows recirculation of the NEPCM suspension. Therefore, since the cavity is not sealed, it is called an open-ended or flow-through cavity.

2.2. Governing equations

To analyze the heat transfer behavior of NEPCMs in natural convection, certain assumptions are made. These include the uniformity and stability of the NEPCM-base fluid mixture, small temperature differences within the cavity, and temperature-independent thermophysical properties. However, density is modeled using the Boussinesq approximation. Additionally, it is assumed that the nanoparticles and base fluid are in local thermal equilibrium, and the flow is steady and incompressible. These assumptions have been widely adopted in similar numerical studies and are considered a reliable approach for analyzing steady-state thermal flows [56]. The fundamental equations that describe the flow and heat transfer of the nanofluid mixture can be written in terms

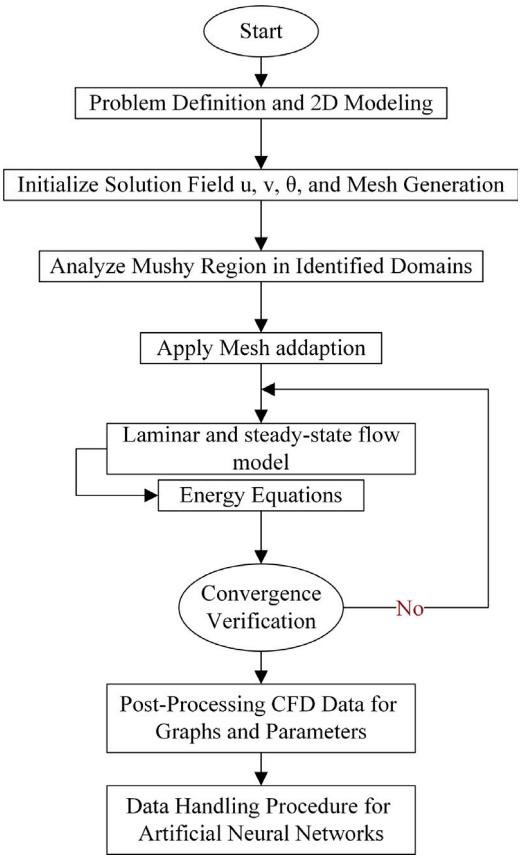

Fig. 2. Flowchart depicting numerical methodology and solution steps.

of conservation of mass, conservation of momentum in the horizontal and vertical directions, and conservation of energy [57].

$$\frac{\partial u}{\partial x} + \frac{\partial v}{\partial y} = 0 \tag{1}$$

$$\rho_m\left(u\frac{\partial u}{\partial x} + v\frac{\partial u}{\partial y}\right) = -\frac{\partial p}{\partial x} + \mu_m\left(\frac{\partial^2 u}{\partial x^2} + \frac{\partial^2 u}{\partial y^2}\right) + g\rho_m\beta_m(T - T_\infty) \tag{2}$$

$$\rho_m\left(u\frac{\partial v}{\partial x} + v\frac{\partial v}{\partial y}\right) = -\frac{\partial p}{\partial y} + \mu_m\left(\frac{\partial^2 v}{\partial x^2} + \frac{\partial^2 v}{\partial y^2}\right) \tag{3}$$

$$(\rho c_p)_m\left(u\frac{\partial T}{\partial x} + v\frac{\partial T}{\partial y}\right) = k_m\left(\frac{\partial^2 T}{\partial x^2} + \frac{\partial^2 T}{\partial y^2}\right) \tag{4}$$

where the x and y directions' velocities are represented by u and v. The gravitational constant is shown by g. In this case, the mixture temperature is T, and the mixture pressure is P. Here, the symbols for volume density, thermal expansion, specific thermal capacity, thermal conductivity, and dynamic viscosity of the mixture are represented by the letters ρ, β, C_p, k, and μ, in that order. The bulk characteristics of the suspension mixture are indicated by the subscript m.

The method for producing entropy, which includes friction entropy creation and thermal entropy generation, is represented by the following equation [58]:

$$\dot{S}'''_{gen} = \dot{S}'''_{gen.H} + \dot{S}'''_{gen.V} = \frac{k_m}{T_0^2}\left[\left(\frac{\partial T}{\partial x}\right)^2 + \left(\frac{\partial T}{\partial y}\right)^2\right] + \frac{\mu_m}{T_0}\left[2\left(\frac{\partial u}{\partial x}\right)^2 + 2\left(\frac{\partial v}{\partial y}\right)^2 + \left(\frac{\partial u}{\partial y} + \frac{\partial v}{\partial x}\right)^2\right] \tag{5}$$

where the entropy generations resulting from the temperature gradient and fluid layer friction are denoted by the letters $\dot{S}'''_{gen.T}$ and $\dot{S}'''_{gen.f}$ in the equation above, respectively. The heat transfer and flow boundary

conditions are specified based on the model details and the schematic diagram shown in Fig. 1.

At the hot wall ($x = 0$) : $u = v = 0, \quad T = T_h$ (6a)

At the opening BC ($x = A_s \times H$) : $P = P_{amb}, \quad T = T_c$ (6b)

At the bottom wall ($y = 0$) : $u = v = 0, \quad \partial T/\partial y = 0$ (6c)

At the top wall ($y = H$) : $u = v = 0, \quad \partial T/\partial y = 0$ (6d)

To solve the governing equations described earlier, the finite volume method is applied along with appropriate boundary conditions. The discretization of the equation utilizes a second-order upwind approach. Additionally, the SIMPLE scheme is employed to handle pressure–velocity coupling.

2.3. Bulk properties of the NEPCM suspension

The PCM is encapsulated in a polymer shell, creating a nano-encapsulated PCM. The suspension is similar to a nanofluid, but instead of simple nanoparticles, NEPCM particles are used. The NEPCM particles are well dispersed in the host fluid (water) and move with it. As the NEPCM nanoparticles are then suspended in water to create an NEPCM suspension. The NEPCM particles move with the host fluid, the PCM core can undergo phase change and store or release latent heat energy. The NEPCM suspension follows through the open cavity in a flow-through system. The suspension density is determined by considering both the base fluid and the dispersed nano-particles, with appropriate weighting [59]:

$$\rho_m = (1-\phi)\,\rho_f + \phi\,\rho_p \tag{7}$$

Here the subscripts (p) and (f) correspond to the particles and base fluid, respectively.

The density of NEPCMs can be determined as follows [60]:

$$\rho_p = \frac{(1+\iota)\,\rho_{co}\,\rho_{sh}}{\rho_{sh} + \iota\,\rho_{co}} \tag{8}$$

The subscripts (sh) and (co) represent the densities of the shell and core of NEPCMs, respectively. The weight ratio of the core to the shell, denoted as ι, is approximately $\iota \approx 0.447$ for the studied materials [61]. Additionally, the heat capacity of the suspension can be calculated using the following expression [62]:

$$C_{p.m} = \frac{(1-\varphi)\,\rho_f\,C_{p.f} + \varphi\,\rho_p\,C_{p.p}}{\rho_m} \tag{9}$$

The overall heat capacity is suggested to follow the subsequent sinusoidal profile in relation to the phase transition of the core of the nano-capsules [63,64]:

$$C_{p.p} = \begin{cases} C_{p.co}, & T < T_f - \frac{T_{Mr}}{2} \\ C_{p.co} + \left\{ \frac{\pi}{2}\left(\frac{h_{sf}}{T_{Mr}} - C_{p.co} \right) \sin\left(\pi \frac{T - \left(T_f - \frac{T_{Mr}}{2}\right)}{T_{Mr}} \right) \right\}, & T_f - \frac{T_{Mr}}{2} < T < T_f + \frac{T_{Mr}}{2} \\ C_{p.co}, & T > T_f + \frac{T_{Mr}}{2} \end{cases} \tag{10}$$

where $T_{Mr} = 0.24$ °C is the temperature interval and T_f is the core's fusion temperature, and the NEPCM core (n-nonadecane) melts and solidifies at 32.12 °C and 31.9 °C, respectively. However, after encapsulation with polyurethane shells, these points shift to 30.54 °C (melting) and 30.78 °C (solidification). Meanwhile, the solution temperature fluctuates between $T_f \pm T_{Mr}/2$ in the nano-capsule cores, which is where the phase transition takes place. Moreover, the latent heat of fusion (h_{sf}) is 211kJ [65,66].

The suspension's volumetric thermal expansion coefficient can be written as Khanafer and Vafai [67]:

$$\beta_m = (1-\varphi)\,\beta_f + \varphi\,\beta_p \tag{11}$$

The linear relations shown below are used to calculate the suspension's dynamic viscosity and thermal conductivity, which is only valid in cases when $\varphi \le 5\%$ [68]:

$$\frac{\mu_m}{\mu_f} = 1 + N_v\varphi \tag{12}$$

$$\frac{k_m}{k_f} = 1 + N_c\varphi \tag{13}$$

where N_c and N_v stand for the numbers for thermal conductivity and dynamic viscosity, respectively.

The values of $N_v = 12.5$ and $N_c = 23.8$ for NEPCMs in water were determined through curve-fitting based on the experimental research conducted by Barlak et al. [69]. Considering these parameters and to ensure system efficiency, it is important to note that an excessive increase in the volume fraction of NEPCM nanoparticles can lead to several issues, including elevated viscosity, a higher likelihood of particle agglomeration, sedimentation, and deposition [70–72]. Therefore, in this study, a commonly used and optimal range below $\varphi \le 5\%$ was selected to maintain thermal performance and ensure practical applicability. The thermophysical properties of the materials applied to the n-Nonadecane core and polyurethane shell that comprised the NEPCM particles are listed in Table 1.

2.4. Nondimensional parameters

In the numerical solution of this problem, two important nondimensional parameters are the well-known Rayleigh and Prandtl numbers. These parameters play a crucial role in characterizing the behavior of the system, which is defined as Ho et al. [74]:

$$Ra = \frac{g\rho_f\beta_f\Delta T H^3}{\alpha_f\mu_f} \tag{14}$$

$$Pr = \frac{\rho_f\mu_f}{\alpha_f} \tag{15}$$

Here, θ_f, λ, and δ denote the non-dimensional fusion temperature, sensible heat capacity ratio, and melting interval, respectively. These parameters are defined as:

$$\theta_f = \frac{T_f - T_c}{T_h - T_c}, \quad \delta = \frac{T_{Mr}}{T_h - T_c}, \quad \lambda = \frac{\left(Cp_{co,l} + lCp_{sh}\right)\rho_{co}\rho_{sh}}{\rho_f C_f\left(\rho_{sh} + l\rho_{co}\right)} \tag{16}$$

where $\Delta T = T_h - T_c$. Moreover, to define the non-dimensional energy terms involved in the melting process, as formulated in Eqs. (7)–(10), the heat capacity ratio C_r, given by Zhang et al. [75]; Öztop et al. [76] and associated with the ratio $\rho_m C_{p.m}/\rho_f C_{p.f}$, would be derived as follows:

$$Cr = (1-\phi) + \phi\frac{\left(Cp_{co,l} + lCp_{sh}\right)\rho_{co}\rho_{sh}}{Cp_f\left(\rho_{sh} + l\rho_{co}\right)\rho_f} + \phi\frac{\left(T_h - T_c\right)}{T_{Mr}} \times \left\{ \frac{\pi\rho_{co}\rho_{sh}}{2Cp_f\left(\rho_{sh} + l\rho_{co}\right)\rho_f}\left(\frac{h_{sh,f} - Cp_{co,l}T_{Mr}}{\left(T_h - T_c\right)} \right) \right\} f \tag{17}$$

here, f represents the dimensionless fusion function defined as:

$$f = \frac{\pi}{2}\sin\left(\frac{\pi}{\delta}\left(\theta - \theta_f + \frac{\delta}{2} \right) \right) \times \begin{cases} 0 & \theta < \theta_f - \frac{\delta}{2} \\ 1 & \theta_f - \frac{\delta}{2} < \theta < \theta_f + \frac{\delta}{2} \\ 0 & \theta > \theta_f + \frac{\delta}{2} \end{cases} \tag{18}$$

As shown in Eq. (17), the expression $\left[\left(\rho_{co}\rho_{sh}\right)\left(h_{sh,f} - Cp_{co,l}T_{Mr}\right)\right] / \left[\left(T_h - T_c\right)\left(Cp_f\left(\rho_{sh} + \iota\rho_{co}\right)\rho_f\right)\right]$ characterizes the contribution of both latent and sensible heat during the melting process. The parameter T_{Mr} stands for the narrow temperature interval within which phase change occurs. Since the magnitude of the sensible heat term, $Cp_{co,l}$, is considerably lower compared to the latent heat, the product $Cp_{co,l}\cdot T_{Mr}$ is considered negligible. Under this assumption, the Ste, is introduced as:

$$Ste = \frac{\rho_f Cp_f\Delta T(\rho_{sh} + \iota\rho_{co})\alpha_f}{h_{sf}\rho_{co}\rho_{sh}} \tag{19}$$

Table 1
Details of the thermophysical properties of the materials used [73].

Materials	ρ (kg/m^3)	μ (1/K)	k (W m^{-1} K^{-1})	C_p (J/kg K)	β (1/K)
Water	997.1	0.00089	0.613	4.1790	0.00021
Polyurethane	786	–	–	1.3177	0.0001728
Nonadecane	721	–	–	2.0370	–

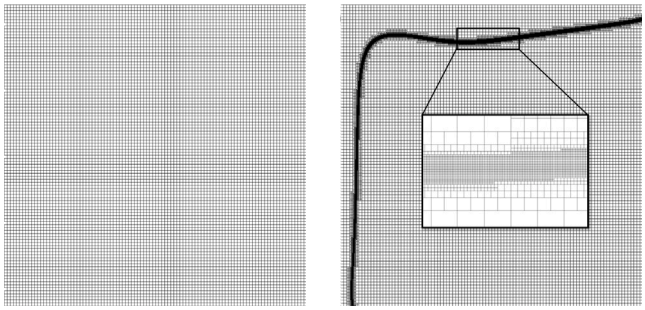

(a) (b)

Fig. 3. Visual representation of the computational mesh used in the study. (a) Shows the initial structured base grid with uniform cell distribution, while (b) illustrates the refined mesh after applying the adaptive mesh refinement algorithm, which enhances resolution in critical regions of phase change.

Furthermore, to establish a non-dimensional representation of the heat capacity ratio, C_r is introduced as follows:

$$C_r = (1-\phi) + \phi\lambda + \frac{\phi}{\delta Ste} f \tag{20}$$

As a main output of these investigations, the local Nusselt number and the average Nusselt number on the hot surface are as Ghalambaz et al. [77]:

$$Nu_y = -\frac{1+N_c\varphi}{2}\frac{\partial\theta}{\partial x} \tag{21}$$

$$Nu_{ave} = \frac{1}{H}\int_0^H Nu_y\, dy \tag{22}$$

where H is the height of the heated wall.

Also, a dimensionless form of the rate of entropy generation and its average over the cavity area are defined as Akbarzadeh et al. [78]:

$$S_g = \frac{\dot{S}'''_{gen} H^2}{k_m} \tag{23}$$

$$S_{ave} = \frac{1}{A}\int S_g\, dA \tag{24}$$

where A is the surface area of the domain.

In order to evaluate the simultaneous effects of heat transfer augmentation and entropy generation deficiency, the efficiency parameter is defined as:

$$\eta = \left(\frac{Nu_{ave}}{Nu_0}\right) \Big/ \left(\frac{S_{ave}}{S_0}\right) \tag{25}$$

where Nu_0 and S_0 are the average Nusselt number and the rate of entropy generation of the plain cavity without any NEPCM, respectively.

2.5. Grid sensitivity analysis

In computational fluid dynamics (CFD) simulations, ensuring grid independence is of critical importance. A mesh sensitivity analysis was performed using three grid resolutions Coarse, Medium, and Fine with the number of elements ranging from 292,797 to 4,055,284.

The two primary criteria for selecting an optimal mesh size were the average Nusselt number (Nu_{ave}) and the relative order error. Initially, a structured and uniform grid was generated as the base mesh Fig. 3(a), where the cell dimensions were equal in both the horizontal and vertical directions. As the solution approached convergence, an adaptive mesh refinement strategy was employed to enhance accuracy in the phase-change regions Fig. 3(b). The adaptive meshing algorithm refined the grid based on the gradient of the heat capacity ratio, and was activated only within the melting range, where sharp changes in thermal properties occur leading to automatic local refinement near the phase-change front. For the grid study, the default values of the dimensionless parameters were set as $A_s = 1.0$, $\varphi = 0.05$, $Ra = 10^5$, $Ste = 0.313$, and $\theta_f = 0.3$. A similar grid sensitivity analysis was also conducted for the critical case (greatest parameter combination), and the results confirmed that the chosen mesh size provides sufficient accuracy. The obtained results in Table 2 indicate that the variation in the average Nusselt number (Nu_{ave}) between the medium and fine grids was minimal less than 0.2%. Consequently, a grid with a base cell size of 1.00×10^{-4} m was selected for the remaining simulations to ensure both accuracy and computational efficiency.

2.6. Validation

To verify the reliability of the code used and the accuracy of the findings, the results are compared to relevant published data for certain applicable scenarios. In the first case, the experimental research of Jahanshahi et al. [79] is selected to simulate the free convective flow in a square cavity at two Rayleigh numbers of 10^5 and 10^6. As the comparison of the average Nusselt number over the heated wall of the present study and the experimental data shows, the present numerical code has acceptable accuracy. In the second case, the free convective flow in open-ended cavities is simulated and compared with the results of Mohamad et al. [26]. Cavities with various aspect ratios are filled with air as the working fluid and exposed to free convection. Fig. 5 shows the comparison of the predicted results for the average Nusselt number of the present study and the results of Mohamad et al. [26], confirming a very good agreement (see Fig. 4).

In the two case study, the problem outlined by Alhashash and Saleh [57] is simulated in order to examine the impact of introducing NEPCMs to the working fluid. The free convective flow in a cavity containing comparable NEPCM particles was numerically solved. Temperature, and capacity ratio contours for the scenarios of $Ra = 10^5$, $Ste = 0.313$, $Pr = 6.2$, $\varphi = 0.5$, and $\theta_f = 0.3$ are compared with the work of Alhashash and Saleh [57]. The findings are in good agreement, as seen in Fig. 5. It is clear that there is only a minor difference between the simulated values and the benchmark data. Thus, the existing numerical computations are considered to be fairly accurate. These numerical simulations, each of which took approximately one hour, were carried out using STAR-CCM+, a finite-volume-based software well-suited for multiphysics and heat transfer problems, on a regular computer with a processor (8 cores, 2.8 GHz) and 32 GB of RAM.

3. Results and discussions

As illustrated in Fig. 2, the numerical solution process begins with problem definition and geometry creation. The governing equations are solved using the Finite Volume Method (FVM), which is chosen for its high accuracy and strong capability in analyzing complex geometries and coupled physical phenomena. Following the initial condition setup, as outlined in the flowchart, the phase-change region of the encapsulated material is defined, along with an adaptive mesh tailored to the computational domain. Subsequently, the governing equations

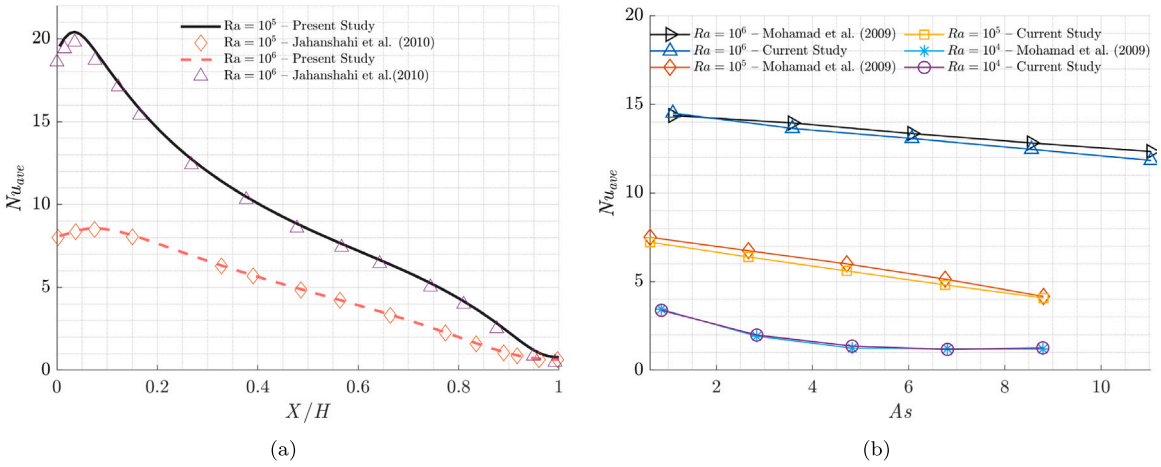

Fig. 4. Comparison of the present simulation results with previous studies: (a) The local Nusselt number distribution over the heated wall of a square cavity is compared with the experimental results reported by Jahanshahi et al. [79]. (b) Average Nusselt number compared with a benchmark solution [26].

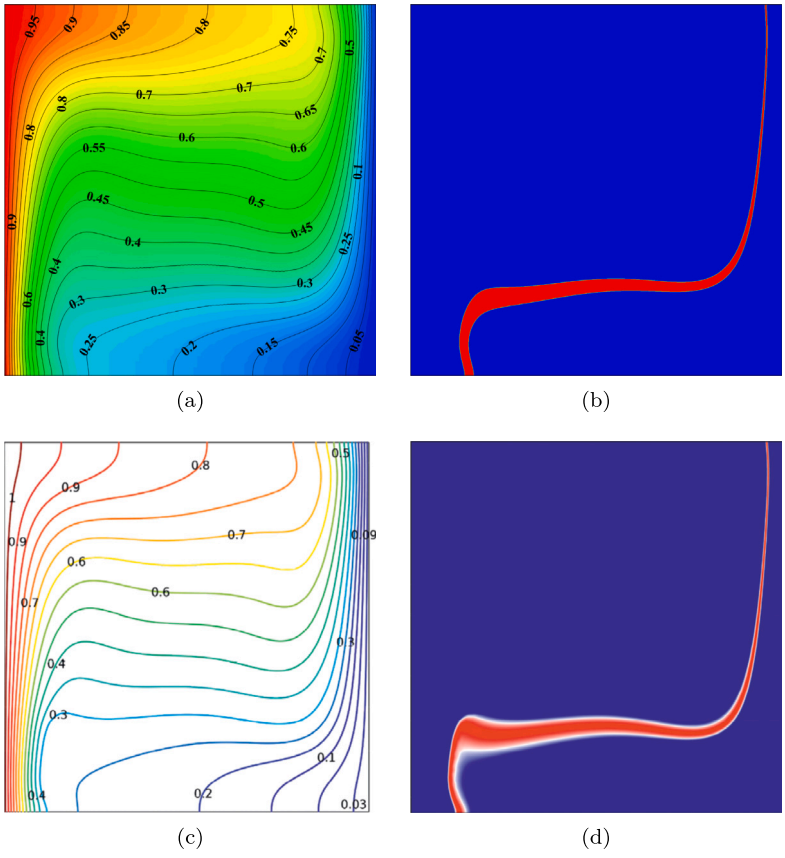

Fig. 5. Comparison between the present simulation results (a, b) and the benchmark problem from Alhashash and Saleh [57] (c, d). The calculated isotherms, and Cr contours are shown for the natural convection of NEPCMs in an enclosure with flat surface at $N_C = N_V = 3.0$, $\phi = 0.05$, $\theta_f = 0.3$, Ste = 0.313, and Ra = 10^5.

Table 2
Grid independence study results for both the base and critical thermal configurations. The base case corresponds to $A_s = 1.0$, $\varphi = 0.05$, $Ra = 10^5$, $Ste = 0.313$, and $\theta_f = 0.3$, while the critical case represents the worst combination with $A_s = 10$, $\varphi = 0.05$, $Ra = 10^6$, $Ste = 0.7$, and $\theta_f = 0.9$.

Case	ID	Grid size (m)	Cell count	Nu_{ave}	Relative error (%)
Base	Coarse	2.00×10^{-4}	292 797	12.70	0.381
	Medium	1.00×10^{-4}	1 032 070	12.65	0.125
	Fine	5.00×10^{-5}	4 055 284	12.63	–
Critical	Coarse	2.00×10^{-4}	855 545	17.48	2.162
	Medium	1.00×10^{-4}	3 262 928	17.11	0.058
	Fine	5.00×10^{-5}	13 563 438	17.10	–

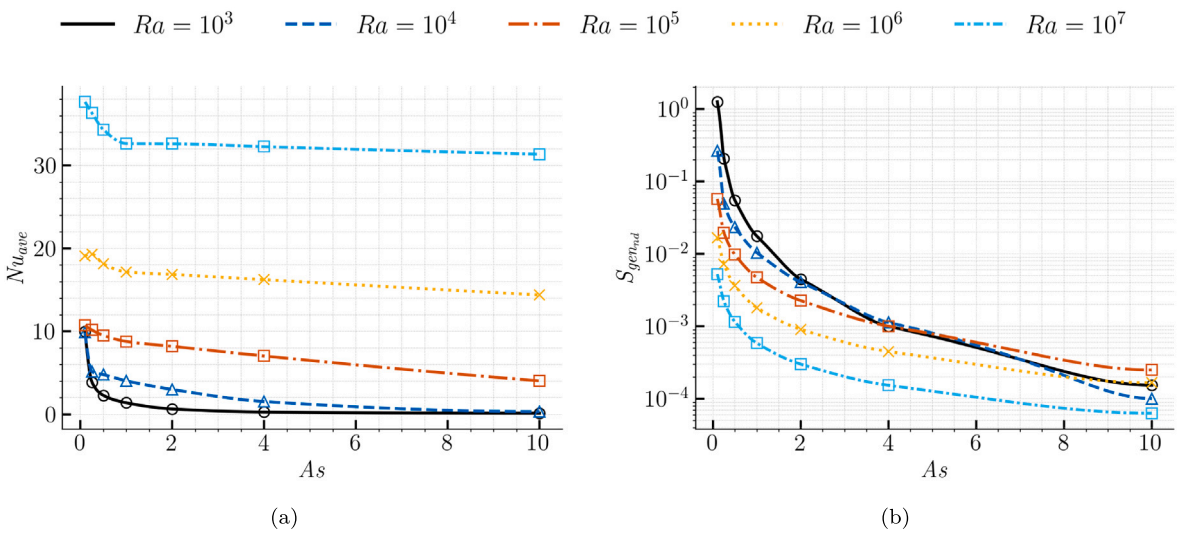

Fig. 6. Variation of average Nusselt number and average normalized entropy generation versus cavity aspect ratio at different Rayleigh numbers. (a) Nu_{ave} at $\varphi = 0.0\%$. (b) $S_{gen_{nd}}$ at $\varphi = 0.0\%$.

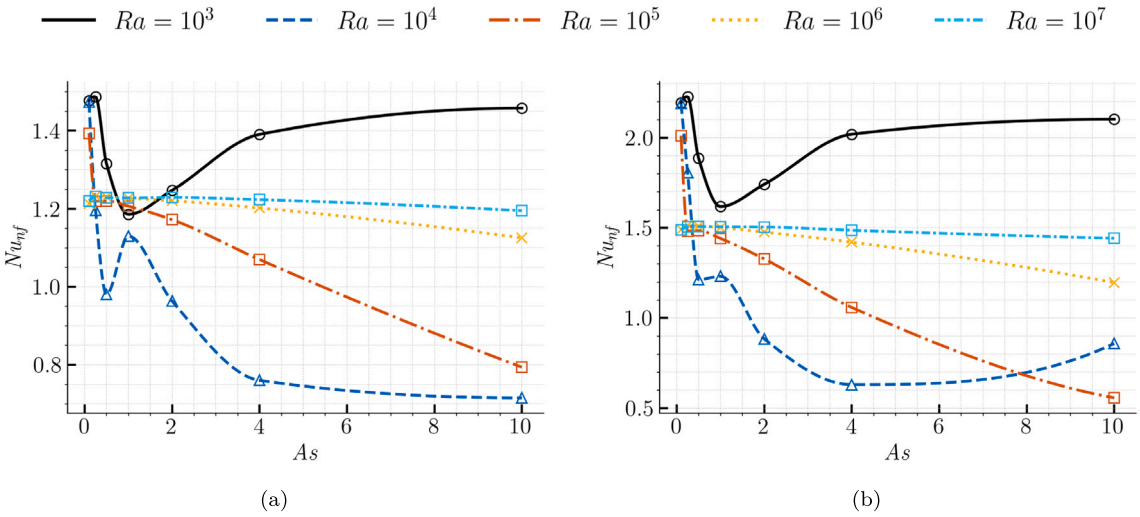

Fig. 7. Nusselt number enhancement versus aspect ratio (A_s) for different NEPCM concentrations and Rayleigh numbers. (a) $\varphi = 2.0\%$. (b) $\varphi = 5.0\%$.

including the continuity equation, the momentum equations, and the energy equation are directly formulated for steady and laminar flow, providing a robust mathematical framework for accurate analysis of flow fields and heat transfer within the mushy region. After achieving convergence, as depicted in the flowchart, the results are prepared for post-processing and subsequently for integration into an ANN. This preparation involves data storage, non-dimensionalization, and preprocessing for effective data handling. With the numerical framework and dataset fully established, the subsequent analysis focuses on the effects of the principal nondimensional parameters, as described below. The associated nondimensional quantities, such as the enclosure's aspect ratio ($0.1 \le A_s \le 10$), fusion temperature ($0.1 \le \theta_f \le 0.7$), Rayleigh number ($10^3 \le Ra \le 10^7$), Stefan number ($0.2 \le Ste \le 0.7$), and concentration of nanoparticles ($0.0 \le \varphi \le 0.05$), were examined using parametric research. The density ratio of the nanoparticles is less than unity since their shell weight is above water and their core weight is below it. Water has a thermal expansion coefficient far higher than these particles. The default values for the nondimensional parameters are taken as follows: $A_s = 1.0$, $\varphi = 0.05$, $Ste = 0.313$, $\theta_f = 0.3$, $Ra = 10^5$, and $Pr = 6.2$. The findings of this study are presented based on these values; if different, the specific value of the nondimensional parameter will be indicated.

The comprehensive analysis of the simulation results reveals key trends regarding the influence of cavity aspect ratio (A_s), Rayleigh number (Ra), and NEPCM concentration (φ) on thermal performance and entropy generation. Overall, the findings demonstrate that increasing the aspect ratio generally leads to reduced heat transfer efficiency, as reflected by a decrease in the average Nusselt number, but simultaneously enhances thermodynamic efficiency by lowering normalized entropy generation. Moreover, higher concentrations of NEPCM further augment heat transfer, particularly at lower aspect ratios and higher Rayleigh numbers. As illustrated in Fig. 6, the average Nusselt number declines with increasing A_s for all studied Rayleigh number ($10^3 \le Ra \le 10^7$). The greatest sensitivity of the Nusselt number to the aspect ratio (As) is observed at low Rayleigh numbers such as $Ra = 10^3$, which also exhibit the steepest reduction with increasing As, whereas higher Rayleigh numbers like $Ra = 10^7$ show a smaller decrease in Nusselt number across the aspect ratio range. Concurrently, normalized entropy generation follows a similar decreasing trend with aspect ratio, indicating improved thermodynamic efficiency

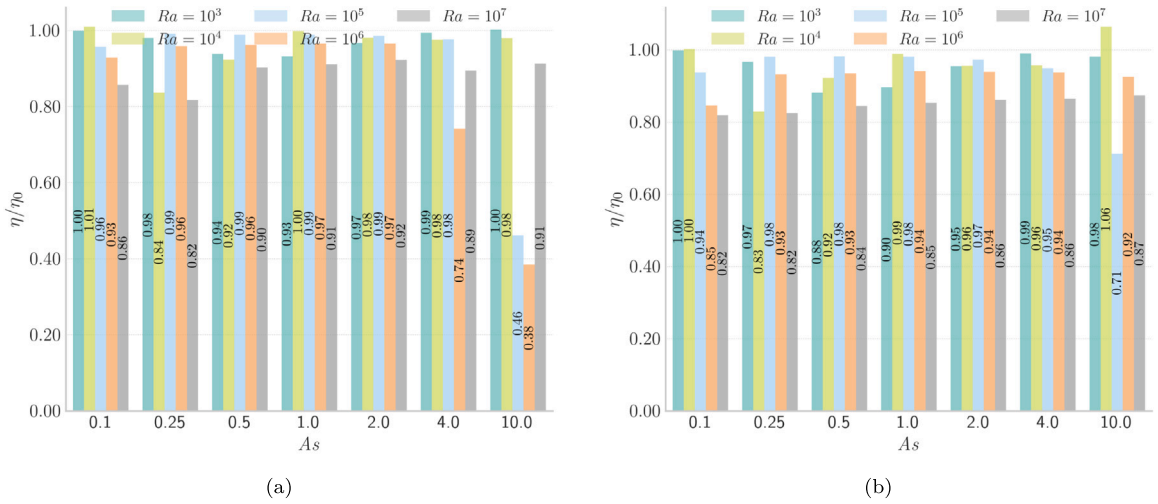

Fig. 8. Comparison of the normalized efficiency parameter (η/η_0) as a function of cavity aspect ratio (A_s) for different Rayleigh number ($10^3 \leq Ra \leq 10^7$) and NEPCM concentrations: (a) $\varphi = 2.0\%$; (b) $\varphi = 5.0\%$.

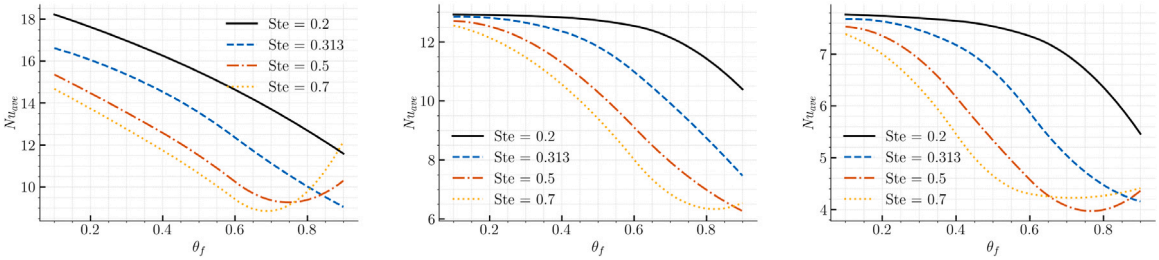

Fig. 9. Effects of Stefan number and fusion temperature on average Nusselt number (Nu) for various aspect ratios.

in elongated cavities. Specifically, $Ra = 10^3$ shows the highest entropy generation at smaller aspect ratios, which diminishes with increasing A_s, while $Ra = 10^6$ consistently maintains lower entropy generation with minimal variation. These observations highlight that, although elongated cavities (higher A_s) are less effective in heat transfer, they offer superior thermodynamic efficiency, especially at higher Rayleigh numbers.

The impact of NEPCM concentration is further elucidated in Fig. 7, which depicts the enhancement of the Nusselt number as a function of aspect ratio for different NEPCM concentrations. For $\varphi = 0.05$ (Fig. 7(b)), the Nusselt number enhancement is highest at the smallest aspect ratio ($A_s = 0.1$) for small to medium range of Rayleigh numbers $10^3 \leq Ra \leq 10^5$ but decreases as A_s increases. At High values of $Ra = 10^6$ and 10^6, , the enhancement remains relatively stable across smaller aspect ratios before declining at higher A_s. This behavior suggests that higher NEPCM concentrations are most beneficial in narrow cavities and at elevated Rayleigh numbers due to increased thermal conductivity and latent heat effects. A similar, albeit less pronounced, pattern is observed for $\varphi = 0.02$ (Fig. 7(a)), where the overall Nusselt number enhancement is lower, underscoring the pivotal role of NEPCM concentration in maximizing thermal performance. In summary, these results underscore the importance of optimizing both geometric As and material (NEPCM concentration) parameters to balance heat transfer and thermodynamic efficiency in NEPCM-based systems. Elongated cavities favor thermodynamic efficiency, while higher NEPCM concentrations and lower aspect ratios are key for maximizing heat transfer. Fig. 8 illustrates the efficiency parameter (η) versus cavity aspect ratio (A_s) at different Rayleigh numbers (Ra) for NEPCM concentrations of: (a) $\varphi = 0.05$, and (b) $\varphi = 0.02$. In Fig. 8(b) for $\varphi = 0.05$, the efficiency parameter peaks at $A_s = 10$ for $Ra = 10^4$ with a value of 1.06, at $A_s = 0.25$ for $Ra = 10^5$ with a value of 0.98, and at $A_s = 0.25$ for $Ra = 10^6$ with a value of 0.93. For $Ra = 10^4$, η decreases from 1.00 at $A_s = 0.1$ to 0.63 at $A_s = 4$, then slightly increases to 0.86 at $A_s = 10$. For $Ra = 10^5$, η decreases from 0.94 at $A_s = 0.1$ to 0.71 at $A_s = 10$. For $Ra = 10^6$, η remains relatively stable around 0.93 for A_s between 0.1 and 1, then decreases to 0.92 at $A_s = 10$. At the lower Rayleigh number of 10^3, η values are generally lower but show a gradual increase with aspect ratio, reflecting conduction-dominated behavior. At the higher Rayleigh number of 10^7, η increases sharply with As, reaching significantly higher values, indicating enhanced thermodynamic efficiency in strongly convective regimes. In Fig. 8(a) for $\varphi = 0.02$, the efficiency parameter peaks at $A_s = 1$ for $Ra = 10^4$ with a value of 1.00, at $A_s = 0.25$ for $Ra = 10^5$ with a value of 0.99, and at $A_s = 0.25$ for $Ra = 10^6$ with a value of 0.96. For $Ra = 10^4$, η decreases from 1.01 at $A_s = 0.1$ to 0.98 at $A_s = 10$. For $Ra = 10^5$, η decreases from 0.96 at $A_s = 0.1$ to 0.46 at $A_s = 10$. For $Ra = 10^6$, η decreases from 0.93 at $A_s = 0.1$ to 0.38 at $A_s = 10$. At $Ra = 10^3$, η remains low with a slight increase as As grows, while at $Ra = 10^7$, η rises significantly with As, indicating improved efficiency in highly convective conditions. These trends suggest that heat transfer augmentation efficiency and entropy generation reduction are maximized at specific aspect ratios. Generally, higher NEPCM concentrations lead to greater efficiency. The observed peaks indicate that there are optimal aspect ratios for maximizing thermal performance, which vary depending on the Rayleigh number and NEPCM concentration. Moreover, Fig. 9 illustrates the effects of the Ste and fusion temperature (θ_f) on the average Nusselt number (Nu) for different aspect ratios ($A_s = 0.25$, 1.0, and 4.0). For $A_s = 0.25$, the trend is especially distinct at $Ste = 0.2$, where the Nusselt number drops significantly from 18.2 at $\theta_f = 0.1$ to 11.6 at $\theta_f = 0.9$. For $A_s = 1.0$, Nu also decreases as θ_f increases, but the decline is more

Table 3
Variation of thermal efficiency $\eta = Nu_{ave}/S_{gen} \times 100$ (%) for different values of As, Ste, and θ_f.

As	Ste	Thermal Efficiency η at various θ_f (%)				
		0.1	0.3	0.5	0.7	0.9
0.25	0.200	22.6	22.5	22.3	22.0	20.1
	0.313	22.6	22.4	22.1	21.8	19.5
	0.500	22.4	22.1	21.8	21.4	18.7
	0.700	22.2	21.9	21.5	21.1	17.8
1.0	0.200	77.4	77.8	78.9	82.3	81.2
	0.313	24.0	24.4	25.5	26.2	22.2
	0.500	7.1	7.4	7.6	7.1	5.9
	0.700	3.0	3.1	3.1	2.4	2.4
4.0	0.200	287.3	287.6	288.8	296.0	295.3
	0.313	88.6	89.0	91.6	91.2	81.2
	0.500	26.0	26.6	26.7	23.6	22.8
	0.700	10.9	11.1	10.2	9.5	9.1

gradual for example, Nu decreases from 12.9 at $\theta_f = 0.1$ to 10.4 at $\theta_f = 0.9$ for $Ste = 0.2$. In the case of $A_s = 4.0$, the reduction in Nu with increasing θ_f is less pronounced; Nu decreases from 7.8 at $\theta_f = 0.1$ to 5.5 at $\theta_f = 0.9$ for $Ste = 0.2$. Higher Ste values generally lead to higher Nu across all aspect ratios, with the variation being more significant for $A_s = 0.25$. In the context of NEPCM, a higher Ste reflects a greater contribution from sensible heat, thus enhancing heat transfer performance. Moreover, lower fusion temperatures typically increase the average Nusselt number, thereby improving thermal performance for different aspect ratios. These findings highlight the importance of optimizing both Ste and θ_f to maximize heat transfer efficiency, with lower θ_f and higher Ste generally resulting in higher Nu, especially for smaller aspect ratios. Such optimization is essential in applications involving NEPCMs, where efficient thermal management is critical.

For more details, Table 3 offer a comprehensive overview of how thermal efficiency η responds to variations in cavity A_s, Ste, and fusion temperature θ_f in NEPCM-assisted systems. The results reveal several broad yet crucial trends that guide the optimal design of such systems. First, the A_s emerges as a dominant factor influencing efficiency. At a low $A_s = 0.25$, thermal efficiency remains relatively stable and modest, hovering around 22% for most cases demonstrating that compact cavities are less sensitive to variations in phase change parameters. For example, even with changes in Ste or fusion temperature, η typically fluctuates within a narrow range (22.6% at $\theta_f = 0.1$ to 20.1% at $\theta_f = 0.9$ for $Ste = 0.2$. As the aspect ratio increases to an intermediate value $A_s = 1.0$, the interplay between Ste and fusion temperature becomes more pronounced.

Here, efficiency can be remarkably high under favorable conditions (exceeding 77% and peaking above 82%), but drops sharply as Ste increases, falling to as low as 2.4% a nearly 34-fold decrease. This dramatic shift highlights the necessity of careful parameter selection for maximizing performance in these geometries. At high aspect ratios $A_s = 4.0$, the system exhibits extraordinary efficiency under low Ste and low to moderate fusion temperatures reaching values up to 296%. However, this advantage is highly contingent on maintaining favorable conditions; as Ste rises, efficiency rapidly declines to below 10%, effectively negating the benefits of geometric elongation. Fig. 10 illustrates the influence of aspect ratio (A_s) on the development of streamlines, isotherms, heat capacity ratio, and non-dimensional entropy generation contours within open-ended enclosures containing 5% NEPCM, at aspect ratios of 0.5, 1.0, and 2.0. The streamlines show that fluid flow patterns become more elongated and spread out as the aspect ratio increases, indicating changes in flow dynamics.

The isotherms reveal that temperature distribution becomes more uniform with increasing aspect ratio, reducing thermal gradients. The heat capacity ratio contours indicate that thermal storage is more concentrated near the center for $A_s = 0.5$, but becomes more distributed as the aspect ratio increases. The non-dimensional entropy generation contours highlight that higher entropy generation is initially concentrated near the heat source for $A_s = 0.5$, but spreads out with increasing aspect ratio, indicating changes in system irreversibilities. These visualizations are crucial for understanding how aspect ratio influences thermal and fluid dynamics in NEPCM-containing enclosures, which is important for optimizing thermal management systems. Fig. 11 exhibits the influence of increasing fusion temperatures on the distribution of streamlines, isotherms, heat capacity ratio, and entropy generation within an enclosure at $Ra = 10^5$, $\varphi = 0.05$, $Ste = 0.313$, and $A_s = 1.0$. As the fusion temperature increases, the streamlines show a reduction in convective strength, becoming less intense and more elongated, particularly near the open-ended right cold side, which facilitates fluid exit and reduces recirculation. The isotherm contours indicate that increasing the fusion temperature leads to a more uniform temperature distribution within the enclosure. This uniformity effectively reduces thermal gradients and enhances the overall heat dispersion, particularly in the vicinity of the open boundary. Correspondingly, the contours of the heat capacity ratio demonstrate that the thermal storage initially concentrated near the heated wall tends to become more evenly distributed throughout the domain with rising fusion temperature. This redistribution signifies an improvement in thermal storage efficiency.

The entropy generation fields reveal that at lower fusion temperatures, entropy production is predominantly localized around the heat source. However, with increasing fusion temperature, the regions of high entropy generation expand and become more uniformly distributed, indicating a reduction in localized irreversibilities. This trend reflects enhanced thermodynamic performance across the enclosure. The role of NEPCMs is central in shaping these outcomes. Due to their inherent ability to enhance thermal conductivity and store latent heat, NEPCMs significantly improve heat transfer mechanisms particularly at lower fusion temperatures where latent heat exchange is more effectively triggered.

As the fusion temperature rises, the latent heat absorption and release processes become more pronounced, contributing to the observed improvements in both temperature distribution and entropy behavior. Fig. 12 illustrates the influence of the Rayleigh number on the evolution of streamlines, isotherms, heat capacity ratio, and entropy generation distribution. At lower Rayleigh numbers (e.g., $Ra \approx 10^4$), the flow is relatively weak, resulting in subtle temperature stratification and limited circulation. As Ra increases to around 10^5, the flow intensifies, leading to stronger circulation patterns and more defined thermal boundary layers, particularly along the right cold surface. This intensification promotes the redistribution of NEPCM particles and enhances thermal interaction in the lower recirculating regions.

At higher Rayleigh numbers ($Ra \approx 10^6$), convective motion becomes dominant, characterized by vigorous circulation and well-developed thermal layers. The onset and extent of the NEPCM phase change are notably influenced by the heating intensity, which expands the phase

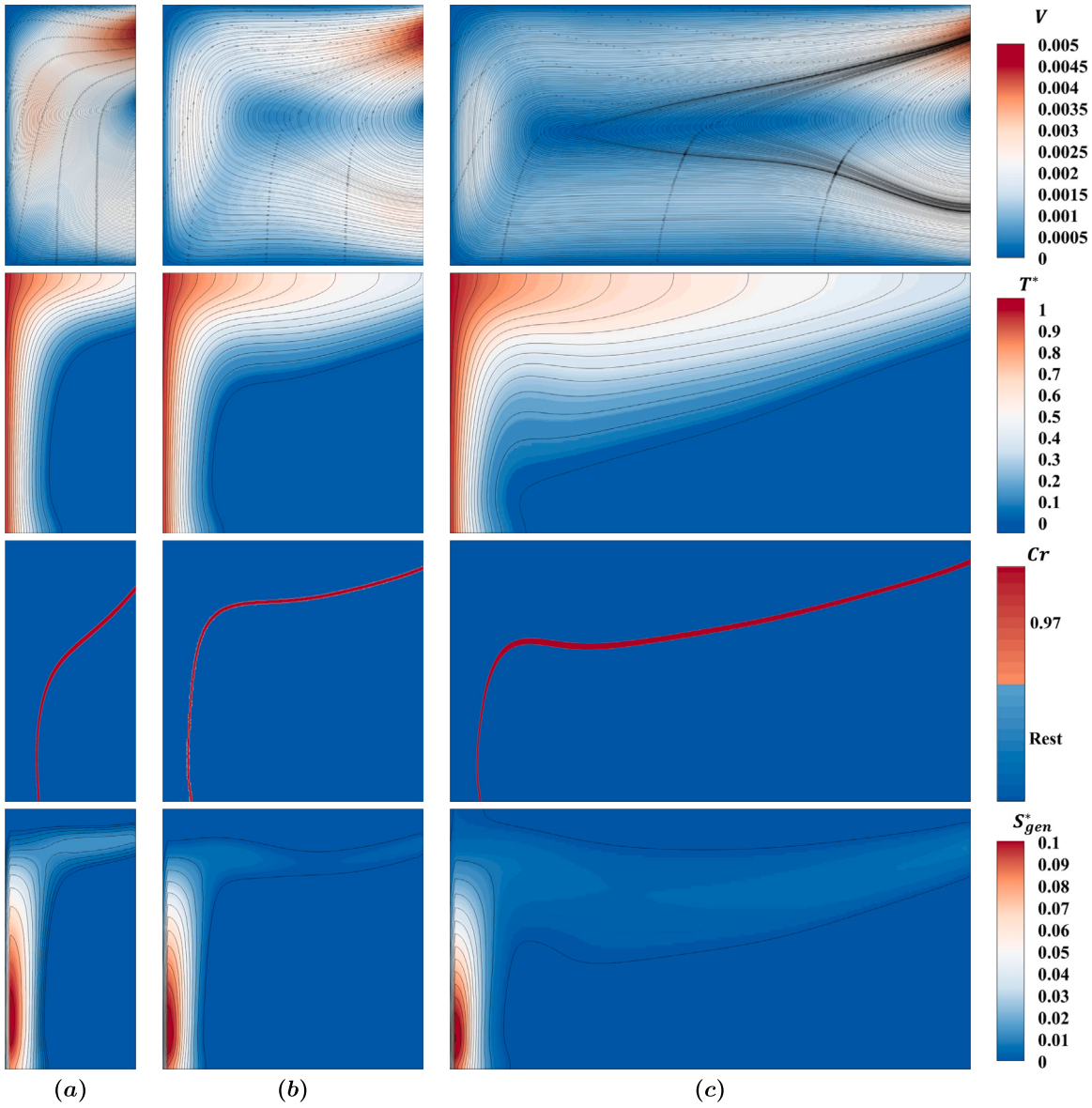

Fig. 10. Influence of aspect ratio on the distribution of the streamlines, isotherms, heat capacity ratio, and non-dimensional entropy generation contours for: (a) $As = 0.5$, (b) $As = 1.0$, (c) $As = 2.0$.

change region in both spatial extent and directional alignment. The contours of heat capacity ratio indicate that higher Ra values promote more localized thermal storage near the heat source. Meanwhile, the entropy generation maps show increased entropy production in these regions, reflecting the trade-off between improved heat transfer and higher irreversibility. These observations highlight the necessity of optimizing the Rayleigh number to achieve a balanced compromise between maximizing heat transfer performance and minimizing entropy generation, particularly in NEPCM-enhanced thermal systems.

3.1. ANN-based prediction

Given the high computational cost associated with traditional numerical simulations, particularly when evaluating the impact of multiple parameters on natural convection of NEPCM suspensions in open cavities, developing a robust predictive model is essential for design optimization and real-time system assessment. In this context, this Section 3.1 provides an ANN model that was developed to predict two key performance indicators: the Nu_{ave} and the overall thermal efficiency of the system. The ANN was trained using simulation data from the validated CFD model described in previous sections. The inputs to the network consisted of the principal dimensionless and physical parameters that significantly influence the system's thermal behavior, namely the Rayleigh number (Ra), cavity A_s, Ste, and fusion temperature. The model outputs were the average Nusselt number and overall thermal efficiency, both of which are critical for assessing heat transfer enhancement and thermodynamic performance. A multilayer feed-forward neural network with a single hidden layer was employed in this study, as this architecture has proven effective for nonlinear regression problems in engineering applications. The number of neurons in the hidden layer, the activation functions, and the data split into training, validation, and testing sets were all optimized to minimize prediction error. The Levenberg–Marquardt backpropagation algorithm was used to train the network, owing to its high efficiency and fast convergence in function approximation tasks. The simulation dataset comprised over 100 cases, covering a wide range of parameter variations $0.25 \leq A_s \leq 4$, $0.2 \leq Ste \leq 0.7$, $0.1 \leq \theta_f \leq 0.9$ at a constant $Ra = 10^5$.

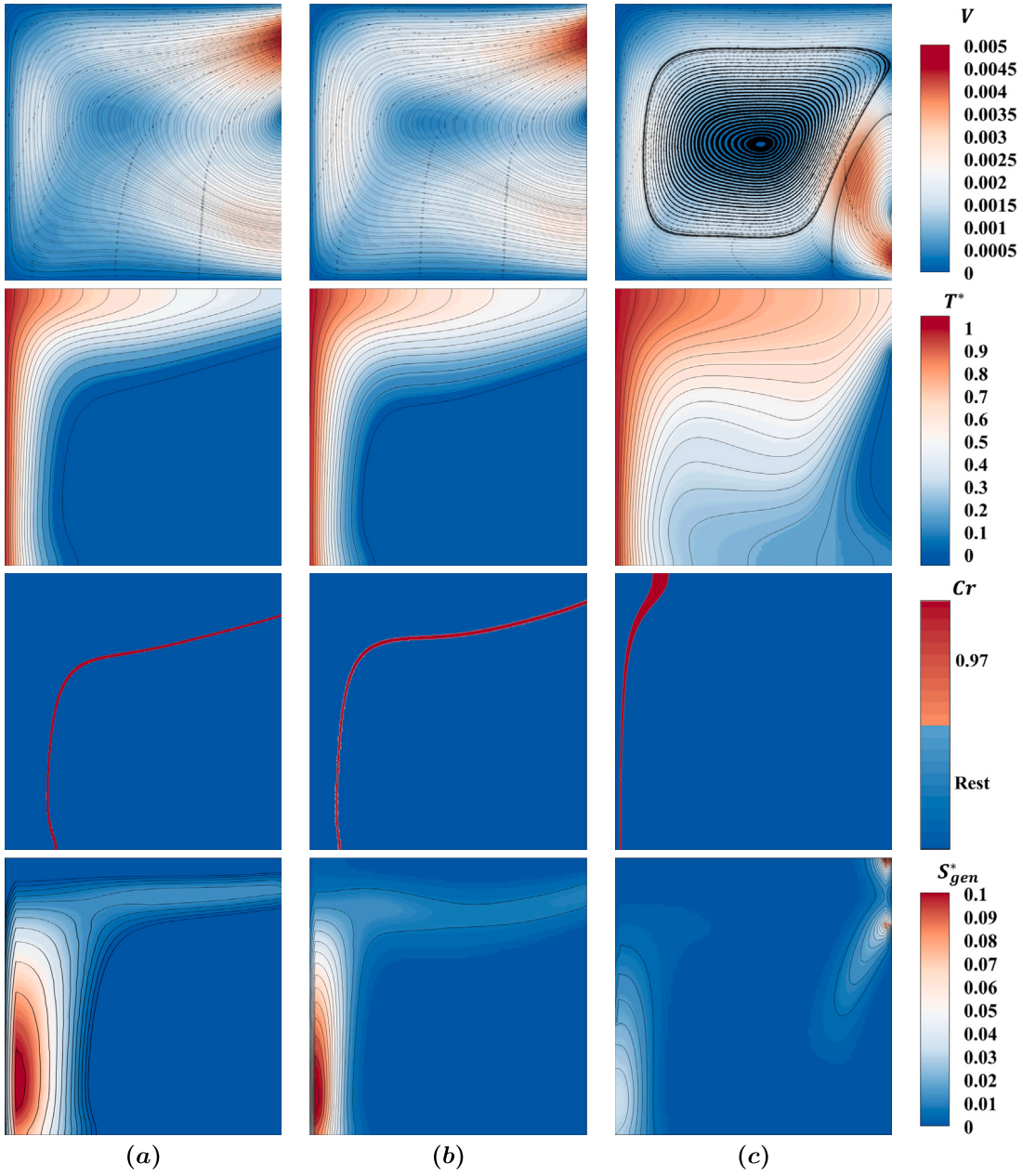

Fig. 11. Influences of the fusion temperature on the streamlines, isotherms, heat capacity ratio, and non-dimensional entropy generation contour for: (a) $\theta_f = 0.1$, (b) $\theta_f = 0.5$, and (c) $\theta_f = 0.9$.

Furthermore, 70% of the data were randomly allocated for training, 15% for validation, and the remaining 15% for testing. In the present study, Fig. 13 presents a well-organized flowchart that illustrates how the numerical results obtained from numerical programming are transferred to the neural network model. As shown, this research employs 10 neurons in the hidden layer and 2 neurons in the output layer to enable accurate prediction of the average Nusselt number and thermal efficiency. Furthermore, a thorough evaluation of the training, validation, and other related processes has been conducted in the continuation of this study.

3.1.1. Comparative visualization of regression performance

This Section 3.1.1 the effectiveness of the feed-forward neural network was systematically analyzed through various statistical error indicators. The network's training utilized the Levenberg–Marquardt backpropagation method, which specifically focuses on reducing the Mean Squared Error (MSE) between predicted outcomes and actual targets. To thoroughly evaluate the performance of the regression model, several metrics were employed, including Root Mean Square Error (RMSE), Correlation Coefficient (R), Coefficient of Determination (R^2), Root Mean Relative Error (RMRE), and Mean Squared Error (MSE). The mathematical definitions and concise descriptions of these criteria are presented below [80].

$$\mathrm{RMSE} = \sqrt{\frac{1}{2N}\sum_{i=1}^{N}\left\|\mathbf{y}_s^{(i)} - \mathbf{y}_a^{(i)}\right\|_2^2} \tag{26}$$

where $\mathbf{y}_s^{(i)} = [\eta_{s,i}, Nu_{s,i}]^T$ and $\mathbf{y} * a^{(i)} = [\eta * a, i, Nu\_a, i]^T$ denote the actual and estimated output vectors for the ith sample, respectively. $\overline{\mathbf{y}_s}$ and $\overline{\mathbf{y}_a}$ represent the mean values of the actual and estimated outputs,

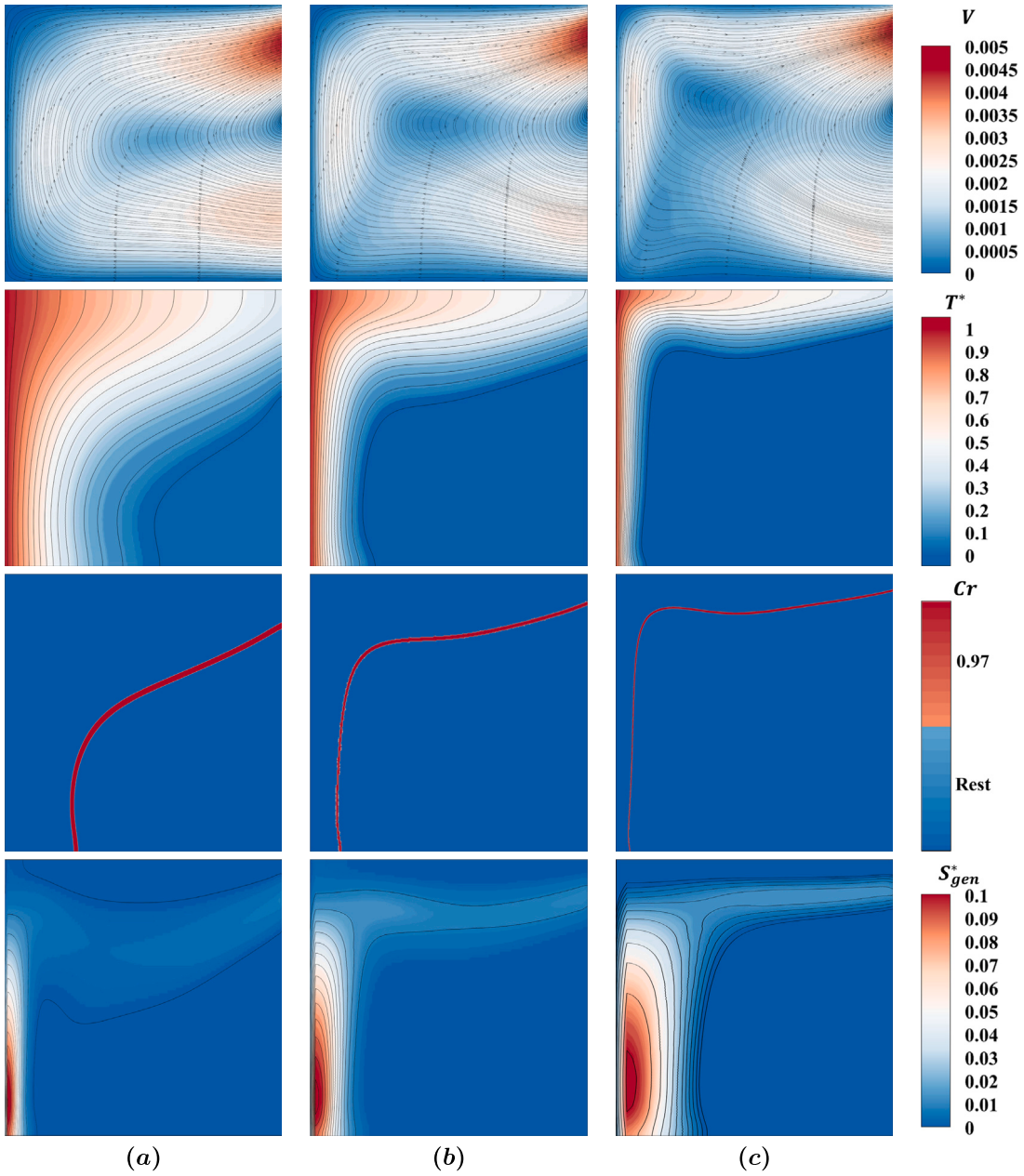

Fig. 12. Influences of the Rayleigh number on the streamlines, isotherms, heat capacity ratio, and non-dimensional entropy generation contour for: (a) $Ra = 10^4$, (b) $Ra = 10^5$, and (c) $Ra = 10^6$.

and N indicates the total number of samples.

$$R = \frac{\sum_{i=1}^{N}\left(\mathbf{y}_s^{(i)} - \overline{\mathbf{y}_s}\right)\cdot\left(\mathbf{y}_a^{(i)} - \overline{\mathbf{y}_a}\right)}{\sqrt{\sum_{i=1}^{N}\left\|\mathbf{y}_s^{(i)} - \overline{\mathbf{y}_s}\right\|_2^2 \sum_{i=1}^{N}\left\|\mathbf{y}_a^{(i)} - \overline{\mathbf{y}_a}\right\|_2^2}} \tag{27}$$

The correlation coefficient (R) quantifies both the strength and direction of the linear association between the predicted and actual outputs, with values approaching 1 signifying a strong positive relationship. In addition, the coefficient of determination (R^2) represents the proportion of variance in the observed outputs that is attributable to the input variables, with higher R^2 values indicating enhanced predictive capability. Complementing these indicators, the Root Mean Relative Error (RMRE) offers a normalized measure of predictive accuracy by evaluating the relative differences between predicted and observed values. The mathematical formulations for R^2 and RMRE are presented below:

$$R^2 = 1 - \frac{\sum_{i=1}^{N}\left\|\mathbf{y}_s^{(i)} - \mathbf{y}_a^{(i)}\right\|_2^2}{\sum_{i=1}^{N}\left\|\mathbf{y}_s^{(i)} - \overline{\mathbf{y}_s}\right\|_2^2} \tag{28}$$

$$\mathrm{RMRE} = \sqrt{\frac{1}{2N}\sum_{i=1}^{N}\left(\left|\frac{\eta_{s,i} - \eta_{a,i}}{\eta_{s,i}}\right| + \left|\frac{Nu_{s,i} - Nu_{a,i}}{Nu_{s,i}}\right|\right)} \tag{29}$$

$$\mathrm{MSE} = \frac{1}{2N}\sum_{i=1}^{N}\left\|\mathbf{y}_s^{(i)} - \mathbf{y}_a^{(i)}\right\|_2^2 \tag{30}$$

The mean squared error quantifies the average squared difference between the predicted and actual values, with lower values indicating better model performance and higher generalization capability. In the present study, the trained ANN model achieved excellent predictive accuracy, as evidenced by $RMSE = 0.002641$, $R^2 = 0.99978$, and

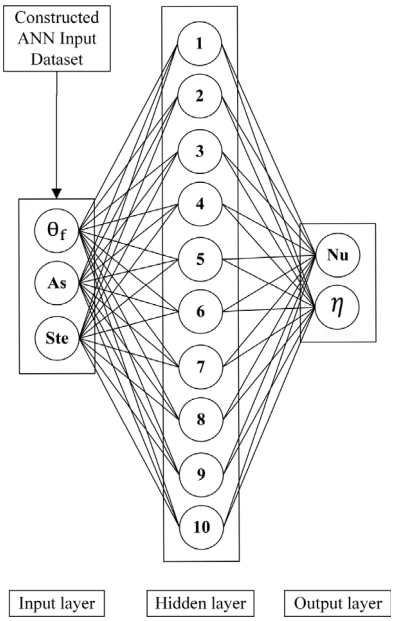

Fig. 13. Architecture of the CFD-ANN model with three input variables, one hidden layer of ten neurons, and two output nodes.

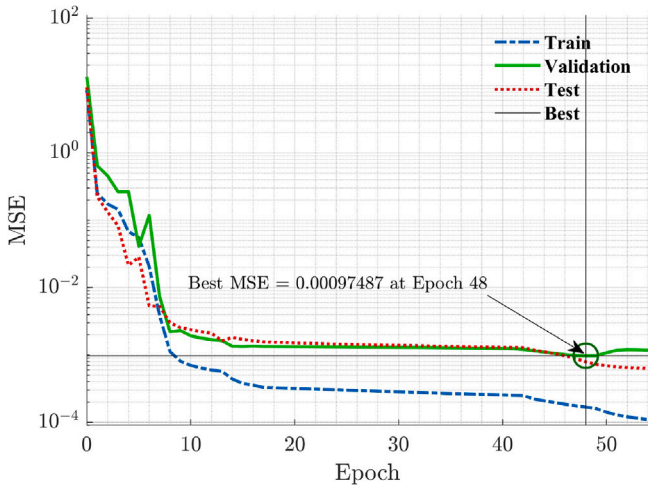

Fig. 14. Training history of MSE showing optimal validation performance 0.00097487 achieved at epoch 48 with early stopping.

$RMRE = 0.045023$. These statistical indicators provide a comprehensive and reliable assessment of the regression performance during both the training and validation phases. They confirm that the trained ANN model is not only highly accurate in its predictions but also exhibits strong reliability and generalizability when exposed to new, unseen data.

This ANN algorithm, as illustrated in Fig. 13, uses three inputs (Ste, θ_f, As) and two outputs (η and Nu_{ave}). A tan-sigmoid transfer function was used for the hidden layer, and a linear transfer function was used for the output layer. The training performance and learning process of this network are depicted in Fig. 14, which illustrates the changes in the MSE for the training, validation, and test datasets throughout the neural network's training epochs. As observed, the MSE decreases rapidly during the initial epochs and then exhibits a more gradual downward trend after approximately 10 epochs. The model achieves its best performance on the validation data at epoch 48, with an MSE of 0.00097487. These improvements in the training process translate into highly accurate predictions by the ANN model, as demonstrated in the subsequent performance evaluations. As Fig. 15 illustrates the performance of the ANN model in predicting outputs based on the training, validation, testing, and overall datasets. In all four plots, the observed data are compared with the model's predicted values. The regression line and prediction trend clearly demonstrate an excellent agreement between the model predictions and the actual data. The very high correlation coefficients for the training (R=0.99972), validation (R=0.99975), testing (R=0.99848), and the entire dataset (R=0.99963) confirm the outstanding accuracy and efficiency of the model across all data subsets. Overall, these plots indicate that the ANN has effectively learned the relationships among the variables and is capable of predicting the outputs with remarkable accuracy, as evidenced by the data points aligning closely along a straight line in all four cases.

3.1.2. Analysis of predicted thermal characteristics by ANN model

In this Section 3.1.2, a comprehensive analysis of the contour plots for the Nu_{ave} and θ_f, based on predictions from the ANN model, is presented. The results clearly demonstrate the significant influence of key parameters such as A_s, relative melting temperature θ_f, and the Ste on the thermal performance of the enclosure filled with encapsulated phase change materials. According to the findings depicted in Fig. 16, increasing A_s from approximately 0.5 to 4 consistently leads to a decrease in the average Nusselt number. Furthermore, comparison across four different Ste values shows that as Ste increases from 0.2 to 0.7, the maximum Nu_{ave} decreases, and regions of high heat transfer are observed over a wider range of parameters, especially for intermediate θ_f values around 0.1 to 0.4.

Additionally, a notable nonlinear relationship between θ_f and Nu_{ave} is evident: at very low and very high θ_f values close to 0.1 and 0.9, the average Nusselt number increases and decreases, respectively. Analysis of Fig. 17 reveals that the parameter A_s plays a decisive role in enhancing η; as A_s increases, the efficiency rises rapidly and almost linearly, with the highest efficiencies occurring at A_s values greater than 3. However, at low Ste values (e.g., 0.2), the efficiency predominantly depends on A_s and is less sensitive to θ_f. As Ste increases to higher values 0.5 and 0.7, the sensitivity of efficiency to changes in θ_f increases, and more complex patterns with multiple local peaks in η appear. This indicates that achieving maximum thermal efficiency requires not only a high A_s but also an optimal selection of θ_f within a specific range. At high Ste values, regions of high efficiency are mainly concentrated at large A_s and intermediate to high θ_f, while certain areas exhibit local drops in efficiency, likely due to the interplay between rapid melting and intense fluid mixing. Overall, these results indicate that the optimal conditions for achieving maximum heat transfer rate Nu_{ave} and maximum thermal efficiency η do not necessarily coincide. For instance, a point with the highest Nu_{ave} may have a lower efficiency compared to another point with a higher A_s but a different θ_f. Therefore, depending on the operational requirements of the system whether prioritizing heat transfer or energy efficiency, the key parameters should be carefully selected. The ANN model employed in this study has successfully identified and predicted optimal regions and nonlinear behaviors of the parameters, providing a robust tool for analyzing and designing complex thermal systems with variable properties. These results can serve as practical guidelines for optimizing the design and control of advanced heat transfer systems with dynamic characteristics.

4. Conclusions

This study presents a comprehensive investigation of natural convection in open cavities filled with NEPCM. Validated two-dimensional CFD simulations were employed in conjunction with ANN modeling. Utilizing NEPCM significantly enhanced heat transfer performance,

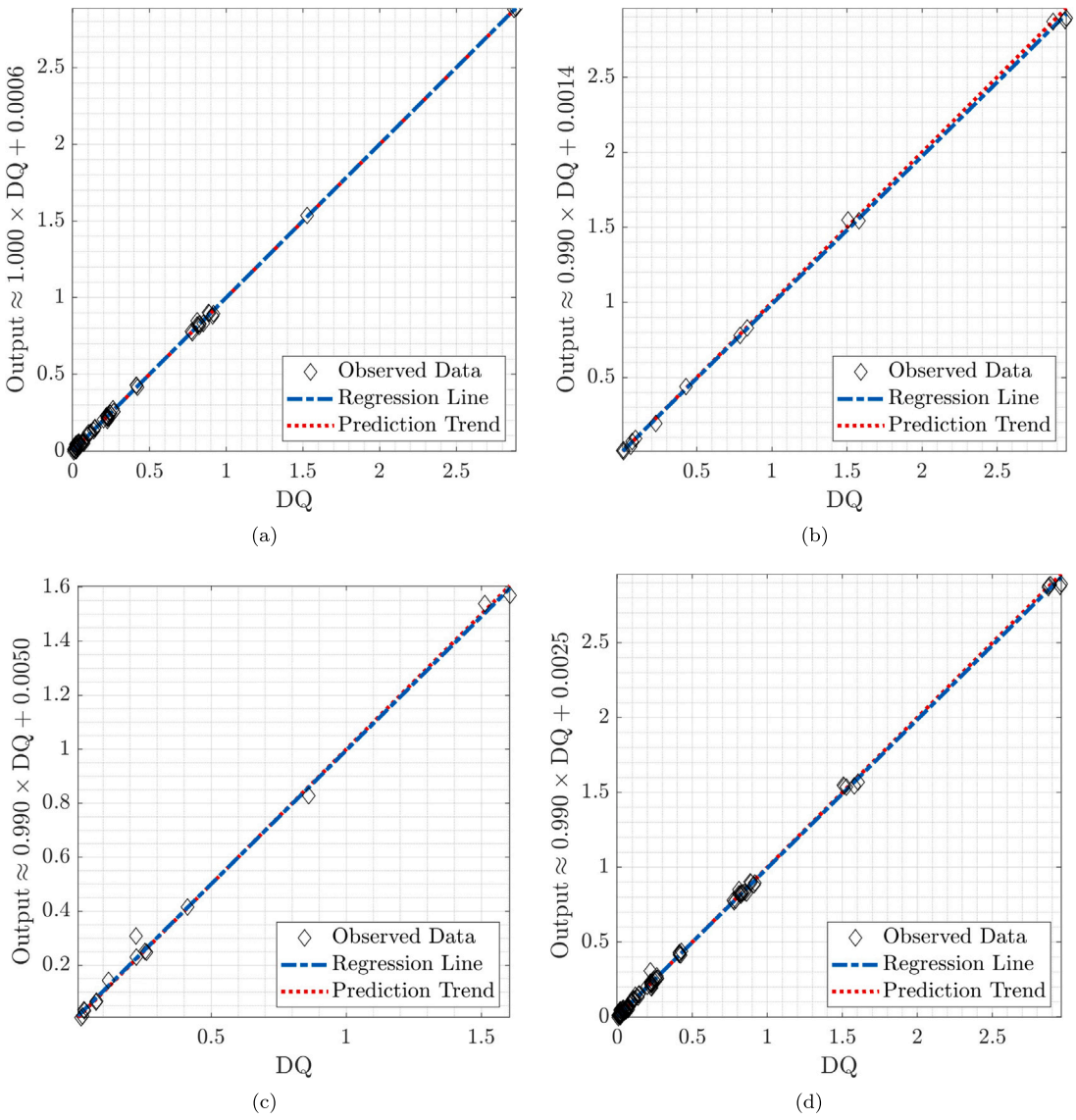

Fig. 15. Regression performance of the ANN model for predicting Nu_{ave} and η, with Desired Quantity (DQ) on the horizontal axis and predicted outputs on the vertical axis. Correlation coefficients (R) are: (a) Training data. (b) Validation data. (c) Testing data. (d) The entire dataset.

with the average Nusselt number increasing by up to 2.19 times compared to the base fluid at a Rayleigh number ($Ra = 10^4$) and an $A_s = 0.1$. However, this enhancement diminishes with increasing aspect ratio, declining to 0.63 at an aspect ratio of $A_s = 4.0$, with a similar trend observed at higher Rayleigh numbers. Detailed analyses indicated that both aspect ratio and NEPCM concentration markedly influence thermal performance. Shallow cavities (aspect ratios between 0.1 and 0.25) exhibited the highest heat transfer improvements, while elongated cavities provided superior thermal efficiency due to a more uniform temperature distribution and reduced thermal gradients. These observations were validated by flow patterns and isotherm plots, underscoring that maximizing heat transfer and thermal efficiency are distinct optimization objectives requiring precise balancing in practical applications. Additionally, the study explored the effects of phase change parameters such as Ste and melting temperature. Higher Stefan numbers positively impacted heat transfer dynamics; for instance, at an aspect ratio of 0.25, increasing the melting temperature from 0.1 to 0.9 reduced the average Nusselt number from 18.2 to 11.6, highlighting the benefit of selecting NEPCMs with lower melting temperatures for rapid heat transfer. A key contribution of this research is the development of a robust ANN-based predictive model, trained with CFD-derived data. The ANN demonstrated exceptional prediction accuracy $R^2 > 0.999$ and minimal mean square error, facilitating rapid parametric studies and real-time optimization. This integrated CFD-ANN approach significantly reduces computational cost compared to conventional CFD methods, where each simulation took approximately one hour, making it a practical tool for efficient system design. Ultimately, achieving optimal thermal performance in NEPCM-based convection systems necessitates a strategic balance between geometric parameters, NEPCM characteristics, and operational conditions. The hybrid CFD-ANN framework presented here not only advances fundamental understanding of NEPCM-induced convection but also provides a powerful, practical means for rapid and precise design, optimization, and implementation of advanced thermal management systems, applicable to passive cooling, latent heat storage, and energy-efficient building technologies. In future research, focusing on the transient behavior of NEPCMs during repeated melting and solidification cycles could significantly enhance the findings of the present study. Investigating the sedimentation trends of nanoparticles over time, the effects of thermal cycling on system performance, and the role of various additives in improving stability are among the key aspects that could lead to a deeper and more accurate understanding of the subject. Such studies

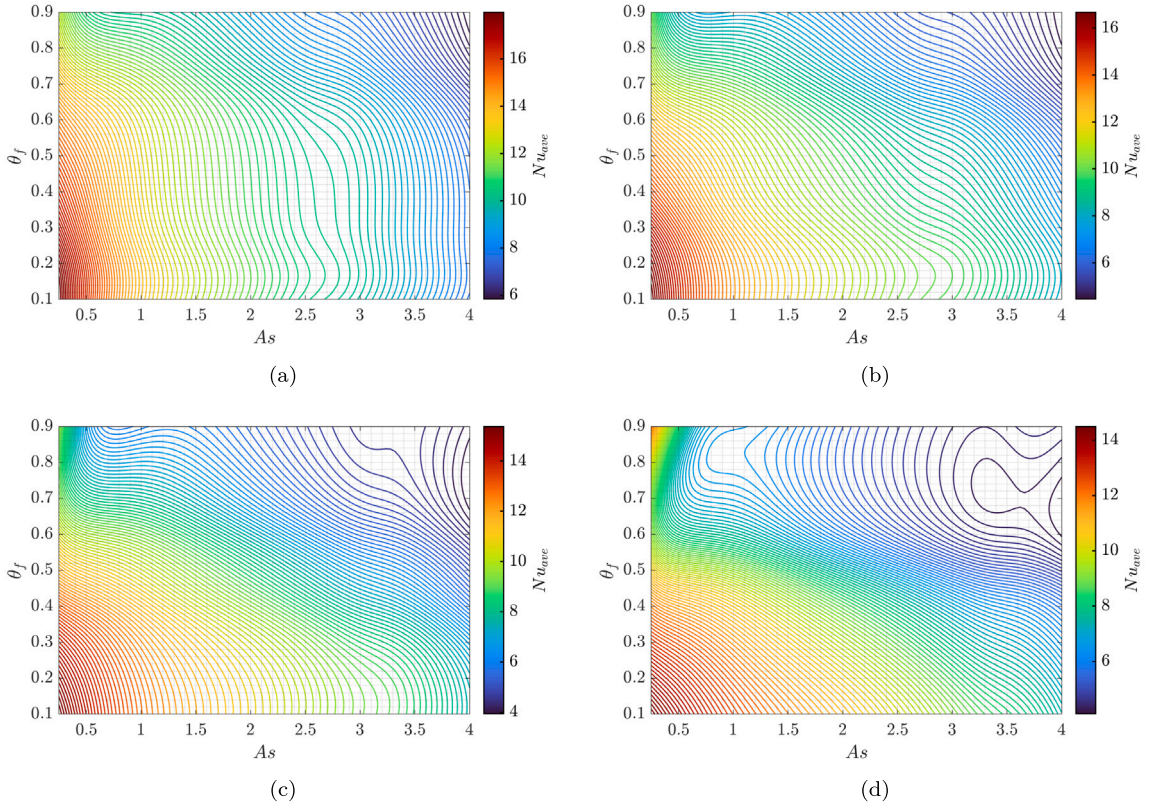

Fig. 16. Contours of average Nusselt number (Nu_{ave}) as functions of Ra, θ_f, and As for $\phi = 5\%$. based on ANN predictions. (a) $Ste = 0.2$. (b) $Ste = 0.313$. (c) $Ste = 0.5$. (d) $Ste = 0.7$.

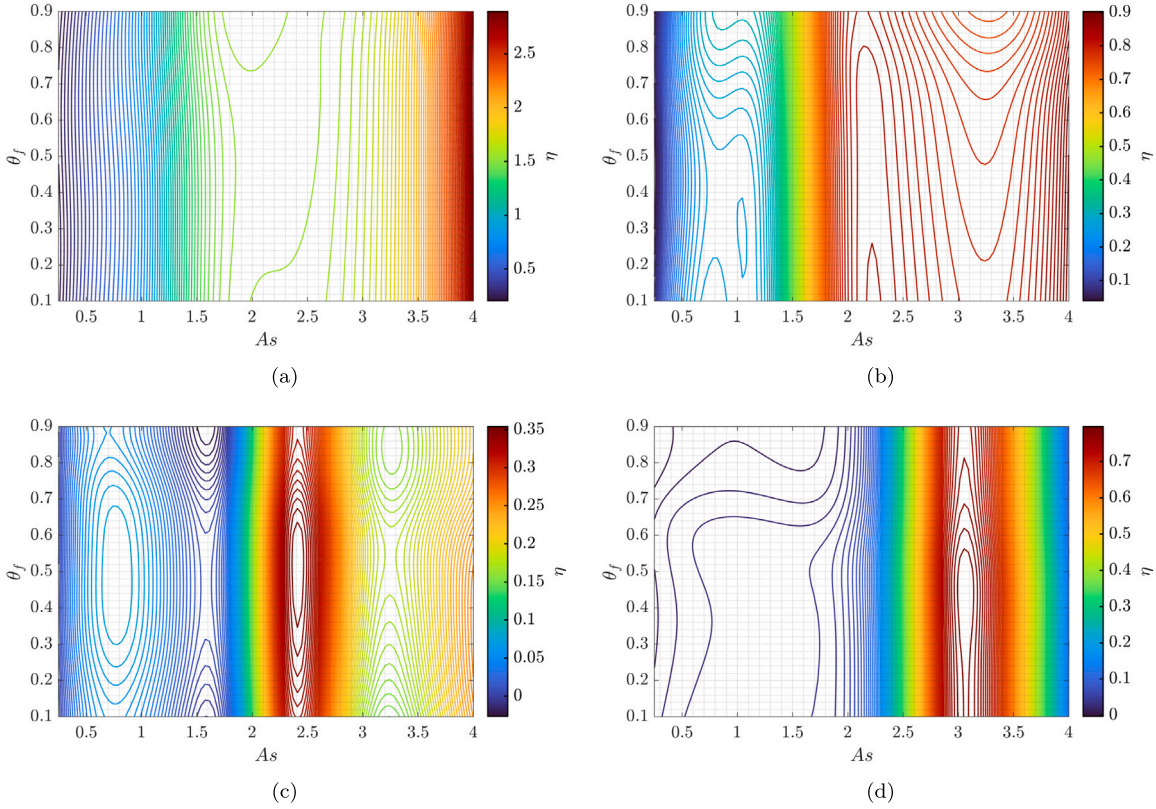

Fig. 17. Contours of thermal efficiency (η) as functions of Ra, θ_f, and As for $\phi = 5\%$, based on ANN predictions. (a) $Ste = 0.2$. (b) $Ste = 0.313$. (c) $Ste = 0.5$. (d) $Ste = 0.7$.

can offer valuable insights into the real-world efficiency and durability of NEPCM-based systems under practical operating conditions.

CRediT authorship contribution statement

Mohammad Abbaszadeh: Resources, Methodology, Conceptualization. **Alireza Timas:** Writing – original draft, Validation. **Mojtaba Mirzaei:** Writing – review & editing, Formal analysis. **Iman Hosseini:** Writing – original draft. **Mohammad Ghalambaz:** Writing – original draft, Supervision.

Declaration of competing interest

The authors declare that they have no known competing financial interests or personal relationships that could have appeared to influence the work reported in this paper.

Data availability

Data will be made available on request.

References

[1] M.H. Abokersh, M. Osman, O. El-Baz, M. El-Morsi, O. Sharaf, Review of the phase change material (PCM) usage for solar domestic water heating systems (SDWHS), Int. J. Energy Res. 42 (2) (2018) 329–357, http://dx.doi.org/10.1002/er.3765, arXiv:https://onlinelibrary.wiley.com/doi/pdf/10.1002/er.3765. URL: https://onlinelibrary.wiley.com/doi/abs/10.1002/er.3765.

[2] J. Jaguemont, N. Omar, P. Van den Bossche, J. Mierlo, Phase-change materials (PCM) for automotive applications: A review, Appl. Therm. Eng. 132 (2018) 308–320, http://dx.doi.org/10.1016/j.applthermaleng.2017.12.097, URL: https://www.sciencedirect.com/science/article/pii/S1359431117319762.

[3] K. Du, J. Calautit, Z. Wang, Y. Wu, H. Liu, A review of the applications of phase change materials in cooling, heating and power generation in different temperature ranges, Appl. Energy 220 (2018) 242–273, http://dx.doi.org/10.1016/j.apenergy.2018.03.005, URL: https://www.sciencedirect.com/science/article/pii/S0306261918303349.

[4] K.B. Saleem, R.J. Mohammed, G.F. Smaisim, Natural convective Cu-water nanofluid flow in isosceles triangular cavity with forced free stream cooled sides and localized heated base, Int. J. Thermofluids 23 (2024) 100766, http://dx.doi.org/10.1016/j.ijft.2024.100766, URL: https://www.sciencedirect.com/science/article/pii/S2666202724002088.

[5] S. Guo, K.X. Cheng, P.S. Lee, Numerical study of the cold finned-tube bundle heat exchanger under natural convection for a novel passive displacement cooling system, Build. Environ. 233 (2023) 110083, http://dx.doi.org/10.1016/j.buildenv.2023.110083, URL: https://www.sciencedirect.com/science/article/pii/S0360132323001105.

[6] M. Matuszczak, K. Nycz, W. Mazurek, P. Krowicki, S. Pietrowicz, D. Pandelidis, Experimental comparison of finned tube heat exchangers for heat rejection under natural convection conditions, Int. Commun. Heat Mass Transfer 154 (2024) 107461, http://dx.doi.org/10.1016/j.icheatmasstransfer.2024.107461, URL: https://www.sciencedirect.com/science/article/pii/S0735193324002239.

[7] A. Zidan, M. Nayak, N. Karimi, A. Sattar Dogonchi, A.J. Chamkha, M.B. Ben Hamida, A.M. Galal, Thermal management and natural convection flow of nano encapsulated phase change material (NEPCM)-water suspension in a reverse T-shaped porous cavity enshrining two hot corrugated baffles: A boost to renewable energy storage, J. Build. Eng. 53 (2022) 104550, http://dx.doi.org/10.1016/j.jobe.2022.104550, URL: https://www.sciencedirect.com/science/article/pii/S2352710222005630.

[8] C. Introini, D. Chiesa, M. Nastasi, E. Previtali, A. Salvini, M. Sisti, X. Wang, A. Cammi, A complete CFD study on natural convection in the TRIGA Mark II reactor, Nucl. Eng. Des. 403 (2023) 112118, http://dx.doi.org/10.1016/j.nucengdes.2022.112118, URL: https://www.sciencedirect.com/science/article/pii/S0029549322004691.

[9] A. Teräsvirta, J. Hyvärinen, Nuclear engineering and design nuclear heat supply system for a small district heating reactor, Nucl. Eng. Des. 426 (2024) 113389, http://dx.doi.org/10.1016/j.nucengdes.2024.113389, URL: https://www.sciencedirect.com/science/article/pii/S0029549324004898.

[10] O. Anuma, M.C. Ndukwu, G. Usoh, E.O. Sam, G. Akpan, L. Oriaku, F. Orji, L. Akuwueke, A.E. Ben, N. Bekkioui, M. Simo-Tagne, F. Abam, Energy and exergy analysis of a natural convection solar greenhouse drier with insulated opaque walls for drying aromatic yellow pepper, Renew. Energy 233 (2024) 121141, http://dx.doi.org/10.1016/j.renene.2024.121141, URL: https://www.sciencedirect.com/science/article/pii/S0960148124012096.

[11] Z.A. Qureshi, H.M. Ali, S. Khushnood, Recent advances on thermal conductivity enhancement of phase change materials for energy storage system: A review, Int. J. Heat Mass Transfer 127 (2018) 838–856, http://dx.doi.org/10.1016/j.ijheatmasstransfer.2018.08.049, URL: https://www.sciencedirect.com/science/article/pii/S0017931018325511.

[12] A. Arshad, M. Jabbal, H. Faraji, P. Talebizadehsardari, M.A. Bashir, Y. Yan, Thermal performance of a phase change material-based heat sink in presence of nanoparticles and metal-foam to enhance cooling performance of electronics, J. Energy Storage 48 (2022) 103882, http://dx.doi.org/10.1016/j.est.2021.103882, URL: https://www.sciencedirect.com/science/article/pii/S2352152X21015474.

[13] N.S. Bondareva, M.A. Sheremet, Effect of the time-dependent volumetric heat flux on heat transfer performance inside a heat sink based on the phase change materials, Clean Technol. Environ. Policy 23 (4) (2021) 1151–1160, http://dx.doi.org/10.1007/s10098-020-01818-x.

[14] M.A. Alomari, A.M. Hassan, A. Alajmi, A.M. Sadeq, F. Alqurashi, M.A. Flayyih, A comprehensive numerical analysis of heat transfer enhancement in NEPCM-water mixtures using oscillating fin and oriented magnetic fields, Int. Commun. Heat Mass Transfer 161 (2025) 108455, http://dx.doi.org/10.1016/j.icheatmasstransfer.2024.108455, URL: https://www.sciencedirect.com/science/article/pii/S073519332401217X.

[15] S. Marzouk, F.A. Almehmadi, A. Aljabr, M.A. Sharaf, T. Alam, D. Dobrotă, Study of effects of constructed fins on melting of PCM in helical coil heat exchanger, Case Stud. Therm. Eng. 68 (2025) 105896, http://dx.doi.org/10.1016/j.csite.2025.105896, URL: https://www.sciencedirect.com/science/article/pii/S2214157X2500156X.

[16] H.M.T. Al-Najjar, J.M. Mahdi, D.O. Bokov, N.B. Khedher, N.K. Alshammari, M.J. Catalan Opulencia, M.A. Fagiry, W. Yaïci, P. Talebizadehsardari, Improving the melting duration of a PV/PCM system integrated with different metal foam configurations for thermal energy management, Nanomaterials 12 (3) (2022) http://dx.doi.org/10.3390/nano12030423, URL: https://www.mdpi.com/2079-4991/12/3/423.

[17] F. Iachachene, Y. Halouane, L. Achab, Heat transfer enhancement in lid-driven cavity with rotating cylinder: Exploring NEPCMs and magnetic field effects, Int. Commun. Heat Mass Transfer 149 (2023) 107095, http://dx.doi.org/10.1016/j.icheatmasstransfer.2023.107095, URL: https://www.sciencedirect.com/science/article/pii/S0735193323004840.

[18] J.V. Raj, R. Harish, Enhanced helical fin designs with sugar Alcohol-based hybrid NEPCM for improved melting and thermal safety in Lithium-Ion battery, Energy Convers. Manag.: X 26 (2025) 101032, http://dx.doi.org/10.1016/j.ecmx.2025.101032, URL: https://www.sciencedirect.com/science/article/pii/S2590174525001643.

[19] F.L. Rashid, A.M.R. Al-Gaheeshi, H.I. Mohammed, A. Ameen, Heat convection in a channel-opened cavity with two heated sources and baffle, Energies 17 (5) (2024) http://dx.doi.org/10.3390/en17051209, URL: https://www.mdpi.com/1996-1073/17/5/1209.

[20] A.F. Khalaf, F.L. Rashid, A. Basem, M.H. Abbas, Numerical analysis in a lid-driven square cavity with hemispherical obstacle in the bottom, Math. Model. Eng. Probl. 9 (6) (2022) 1639–1647, http://dx.doi.org/10.18280/mmep.090625.

[21] K.M. Gangawane, R.P. Bharti, S. Kumar, Lattice Boltzmann analysis of effect of heating location and Rayleigh number on natural convection in partially heated open ended cavity, Korean J. Chem. Eng. 32 (8) (2015) 1498–1514, http://dx.doi.org/10.1007/s11814-014-0361-3.

[22] A. Andreozzi, O.M. and, Numerical investigation on the steady state natural convection in a horizontal open-ended cavity with a heated upper wall, Numer. Heat Transf. Part A: Appl. 57 (7) (2010) 453–472, http://dx.doi.org/10.1080/10407781003684324.

[23] O. Manca, B. Morrone, S. Nardini, Effect of transversal aspect ratio on natural convection inside open-ended cavities with uniformly heated horizontal walls, in: ASME International Mechanical Engineering Congress and Exposition, 26669, American Society of Mechanical Engineers, 1999, pp. 177–189.

[24] A.K. Hussein, A.A.R.A. Hussein, A. Abidi, M.A. Ismael, A.B. Mahdi, B.S. Bashar, F.L. Rashid, R.Z. Homod, O. Younis, L. Kolsi, A.J. Chamkha, A review of convective heat transfer in cavity-channel assemblies, Sci. Iran. (2023) http://dx.doi.org/10.24200/sci.2023.61315.7246, URL: https://scientiairanica.sharif.edu/article_23342.html.

[25] F.L. Rashid, A.M.R. Al-Gaheeshi, M. Alhwayzee, B. Ali, N.A. Shah, J.D. Chung, Mixed convection in a horizontal channel–cavity arrangement with different heat source locations, Mathematics 11 (6) (2023) http://dx.doi.org/10.3390/math11061428, URL: https://www.mdpi.com/2227-7390/11/6/1428.

[26] A. Mohamad, M. El-Ganaoui, R. Bennacer, Lattice Boltzmann simulation of natural convection in an open ended cavity, Int. J. Therm. Sci. 48 (10) (2009) 1870–1875, http://dx.doi.org/10.1016/j.ijthermalsci.2009.02.004, URL: https://www.sciencedirect.com/science/article/pii/S1290072909000313.

[27] A. Sanjari, M. Abbaszadeh, A. Abbassi, Lattice Boltzmann simulation of free convection in an inclined open-ended cavity partially filled with fibrous porous media, J. Porous Media 21 (12) (2018).

[28] A. Ait Haj Said, M. Elfagrich, O. Abounachit, Numerical investigation of free convection through a horizontal open-ended axisymmetric cavity, Indian J. Sci. Technol. 14 (13) (2021) 1081–1096.

[29] R. Chaabane, A. Jemni, N.A.C. Sidik, H.W. Xian, Numerical study of magneto-hydrodynamic free convection heat transfer and fluid flow, in: M.Y. Ismail, M.S. Mohd Sani, S. Kumarasamy, M.A. Hamidi, M.S. Shaari (Eds.), Technological Advancement in Mechanical and Automotive Engineering, Springer Nature Singapore, Singapore, 2023, pp. 547–564.

[30] J.M. Mahdi, H.M.T. Al-Najjar, H. Togun, N. Biswas, M. Boujelbene, S. Alshammari, P. Talebizadehsardari, Year-round performance evaluation of photovoltaic-thermal collector with nano-modified phase-change material for building application in an arid desert climate zone, Energy Build. 320 (2024) 114597, http://dx.doi.org/10.1016/j.enbuild.2024.114597, URL: https://www.sciencedirect.com/science/article/pii/S0378778824007138.

[31] H.F. Öztop, H. Coşanay, F. Selimefendigil, N. Abu-Hamdeh, Analysis of melting of phase change material block inserted to an open cavity, Int. Commun. Heat Mass Transfer 137 (2022) 106240, http://dx.doi.org/10.1016/j.icheatmasstransfer.2022.106240, URL: https://www.sciencedirect.com/science/article/pii/S0735193322003621.

[32] S.A. Albdour, Z. Haddad, O.Z. Sharaf, A. Alazzam, E. Abu-Nada, Micro/nano-encapsulated phase-change materials (ePCMs) for solar photothermal absorption and storage: Fundamentals, recent advances, and future directions, Prog. Energy Combust. Sci. 93 (2022) 101037, http://dx.doi.org/10.1016/j.pecs.2022.101037, URL: https://www.sciencedirect.com/science/article/pii/S0360128522000442.

[33] E.J. D'Oliveira, S.C.C. Pereira, D. Groulx, U. Azimov, Thermophysical properties of Nano-enhanced phase change materials for domestic heating applications, J. Energy Storage 46 (2022) 103794, http://dx.doi.org/10.1016/j.est.2021.103794, URL: https://www.sciencedirect.com/science/article/pii/S2352152X21014651.

[34] J. Paul, K. Kadirgama, M. Samykano, A. Pandey, V. Tyagi, A comprehensive review on thermophysical properties and solar thermal applications of organic nano composite phase change materials, J. Energy Storage 45 (2022) 103415, http://dx.doi.org/10.1016/j.est.2021.103415, URL: https://www.sciencedirect.com/science/article/pii/S2352152X21011014.

[35] S.K. Pathak, V. Tyagi, K. Chopra, R. Rejikumar, A. Pandey, Integration of emerging PCMs and nano-enhanced PCMs with different solar water heating systems for sustainable energy future: A systematic review, Sol. Energy Mater. Sol. Cells 254 (2023) 112237, http://dx.doi.org/10.1016/j.solmat.2023.112237, URL: https://www.sciencedirect.com/science/article/pii/S0927024823000582.

[36] F. Khlissa, M. Mhadhbi, W. Aich, A.K. Hussein, M. Alhadri, F. Selimefendigil, H.F. Öztop, L. Kolsi, Recent advances in nanoencapsulated and nano-enhanced phase-change materials for thermal energy storage: A review, Processes 11 (11) (2023) http://dx.doi.org/10.3390/pr11113219, URL: https://www.mdpi.com/2227-9717/11/11/3219.

[37] M. Ghufran, D. Huitink, Advances in encapsulated phase change materials for integration in thermal management applications, Emergent Mater. (2025) http://dx.doi.org/10.1007/s42247-025-01160-2.

[38] A.M. Hassan, M.A. Alomari, Q.H. Al-Salami, F. Alqurashi, M.A. Flayyih, A.M. Sadeq, Numerical analysis of MHD combined convection for enhanced CPU cooling in NEPCM-filled a trapezoidal cavity, Int. Commun. Heat Mass Transfer 159 (2024) 108343, http://dx.doi.org/10.1016/j.icheatmasstransfer.2024.108343, URL: https://www.sciencedirect.com/science/article/pii/S0735193324011059.

[39] C. Timuralp, E. Ercan, U. Ercetin, A. Aygun, E. Esra Altuner, F. Sen, Nanoencapsulation of phase change material with CuO nanoparticles: Development of thermal properties for energy storage, Inorg. Chem. Commun. 170 (2024) 113258, http://dx.doi.org/10.1016/j.inoche.2024.113258, URL: https://www.sciencedirect.com/science/article/pii/S1387700324012474.

[40] S. Hussain, P. Jayavel, B. Almutairi, K. Ramesh, Investigation of MHD oxytactic microorganisms with NEPCMs in rectotrapezoidal enclosure with FEM: Applications to energy storage technologies, J. Magn. Magn. Mater. 592 (2024) 171808, http://dx.doi.org/10.1016/j.jmmm.2024.171808, URL: https://www.sciencedirect.com/science/article/pii/S0304885324000982.

[41] S. Ahmad, K. Ali, T. Sajid, U. Bashir, F. Lafta Rashid, R. Kumar, M.R. Ali, A.S. Hendy, A. Darvesh, A novel vortex dynamics for micropolar fluid flow in a lid-driven cavity with magnetic field localization – A computational approach, Ain Shams Eng. J. 15 (2) (2024) 102448, http://dx.doi.org/10.1016/j.asej.2023.102448, URL: https://www.sciencedirect.com/science/article/pii/S2090447923003374.

[42] P. Sudarsana Reddy, P. Sreedevi, M. Ghalambaz, Heat transfer investigation of nano - Encapsulated phase change materials (NEPCMs) in a thermal energy storage device, Appl. Therm. Eng. 250 (2024) 123495, http://dx.doi.org/10.1016/j.applthermaleng.2024.123495, URL: https://www.sciencedirect.com/science/article/pii/S1359431124011633.

[43] P. Sreedevi, P.S. Reddy, Flow and heat transfer of thermally and chemically radiative Nano-Encapsulated Phase Change Materials (NEPCMs) inside a permeable latent heat thermal energy storage device, Int. Commun. Heat Mass Transfer 163 (2025) 108748, http://dx.doi.org/10.1016/j.icheatmasstransfer.2025.108748, URL: https://www.sciencedirect.com/science/article/pii/S0735193325001733.

[44] Z.-R. Li, G.-T. Fu, L.-W. Fan, Synergistic effects of nano-enhanced phase change material (NePCM) and fin shape on heat storage performance of a finned shell-and-tube unit: An experimental study, J. Energy Storage 45 (2022) 103772, http://dx.doi.org/10.1016/j.est.2021.103772, URL: https://www.sciencedirect.com/science/article/pii/S2352152X21014456.

[45] H.M. Elshehabey, N. Alsedias, A.M. Aly, Artificial intelligence-based ISPH simulation for mass and heat transmission of nano-enhanced phase change material in a porous helix with partial sources, Int. Commun. Heat Mass Transfer 155 (2024) 107563, http://dx.doi.org/10.1016/j.icheatmasstransfer.2024.107563, URL: https://www.sciencedirect.com/science/article/pii/S0735193324003257.

[46] A.M. Aly, M.A. Alotaibi, AI-integrated ISPH framework for enhanced heat and mass transfer in NEPCM systems within porous wavy cylindrical annuli, J. Energy Storage 108 (2025) 115113, http://dx.doi.org/10.1016/j.est.2024.115113, URL: https://www.sciencedirect.com/science/article/pii/S2352152X24046991.

[47] J. Fan, L. Fang, J. Wu, Y. Guo, Q. Dai, From brain science to artificial intelligence, Engineering 6 (3) (2020) 248–252, http://dx.doi.org/10.1016/j.eng.2019.11.012, URL: https://www.sciencedirect.com/science/article/pii/S2095809920300035.

[48] M. Gao, F. zhong Sun, S. jun Zhou, Y. tao Shi, Y. bin Zhao, N. hua Wang, Performance prediction of wet cooling tower using artificial neural network under cross-wind conditions, Int. J. Therm. Sci. 48 (3) (2009) 583–589, http://dx.doi.org/10.1016/j.ijthermalsci.2008.03.012, URL: https://www.sciencedirect.com/science/article/pii/S1290072908000744.

[49] J. Schmidhuber, Deep learning in neural networks: An overview, Neural Netw. 61 (2015) 85–117, http://dx.doi.org/10.1016/j.neunet.2014.09.003, URL: https://www.sciencedirect.com/science/article/pii/S0893608014002135.

[50] S.A. Kalogirou, Applications of artificial neural-networks for energy systems, Appl. Energy 67 (1) (2000) 17–35, http://dx.doi.org/10.1016/S0306-2619(00)00005-2, URL: https://www.sciencedirect.com/science/article/pii/S0306261900000052.

[51] M.A. Alotaibi, W. Alhejaili, A.M. Aly, S. Almalki, Magnetic field influence on heat transfer of NEPCM in a porous triangular cavity with a cold fin and partial heat sources: AI analysis combined with ISPH method, Alex. Eng. J. 119 (2025) 345–358, http://dx.doi.org/10.1016/j.aej.2025.01.080, URL: https://www.sciencedirect.com/science/article/pii/S1110016825001061.

[52] H. Upreti, Z. Uddin, M. Vaseem, Unsupervised AI-driven numerical study of flow and heat transfer analysis of nano-encapsulated phase change material nanofluid over wedge, AI Therm. Fluids 2–3 (2025) 100009, http://dx.doi.org/10.1016/j.aitf.2025.100009, URL: https://www.sciencedirect.com/science/article/pii/S3050585225000084.

[53] T. Tayebi, R. Ali, M. Kouki, M. Nayak, A.M. Galal, Neural network modeling of non-Newtonian NEPCMs suspension in a non-Darcy porous medium under LTNE conditions, J. Taiwan Inst. Chem. Eng. 167 (2025) 105897, http://dx.doi.org/10.1016/j.jtice.2024.105897, URL: https://www.sciencedirect.com/science/article/pii/S1876107024005558.

[54] N. Alsedias, A.M. Aly, N. Biswas, Exothermic reaction on non-Newtonian NEPCM over ellipses in a curved channel: Hybrid ISPH method and artificial intelligence, J. Energy Storage 101 (2024) 113762, http://dx.doi.org/10.1016/j.est.2024.113762, URL: https://www.sciencedirect.com/science/article/pii/S2352152X24033486.

[55] A.M. Hassan, M.A. Alomari, A. Alajmi, A.M. Sadeq, F. Alqurashi, M.A. Flayyih, Enhanced natural convection in a U-shaped baffled cavity: Synergistic effects of magnetic fields and wall oscillations on Nano-encapsulated PCM, Int. Commun. Heat Mass Transfer 165 (2025) 109051, http://dx.doi.org/10.1016/j.icheatmasstransfer.2025.109051, URL: https://www.sciencedirect.com/science/article/pii/S0735193325004774.

[56] X. Wang, R.H. Rasheed, B. Keivani, D.J. Jasim, A.J. Sultan, S. Hamedi, H. Kazemi-Varnamkhasti, S. Salahshour, D. Toghraie, Thermal performance of forced convection of water- NEPCM nanofluid over a semi-cylinder heat source, Case Stud. Therm. Eng. 55 (2024) 104149, http://dx.doi.org/10.1016/j.csite.2024.104149, URL: https://www.sciencedirect.com/science/article/pii/S2214157X24001801.

[57] A. Alhashash, H. Saleh, Impact of surface undulation on flow and heat transfer characteristics in an enclosure filled with nanoencapsulated phase change materials (NEPCMs), Math. Probl. Eng. 2021 (1) (2021) 8899995, http://dx.doi.org/10.1155/2021/8899995, arXiv:https://onlinelibrary.wiley.com/doi/pdf/10.1155/2021/8899995. URL: https://onlinelibrary.wiley.com/doi/abs/10.1155/2021/8899995.

[58] S. Mahmud, A. Islam, Laminar free convection and entropy generation inside an inclined wavy enclosure, Int. J. Therm. Sci. 42 (11) (2003) 1003–1012, http://dx.doi.org/10.1016/S1290-0729(03)00076-0, URL: https://www.sciencedirect.com/science/article/pii/S1290072903000760.

[59] M. Abbaszadeh, M.H. Montazeri, M. Mirzaie, Heat transfer and thermal efficiency enhancement using twisted tapes in sinusoidal wavy tubes with nanofluids: a numerical study, Internat. J. Numer. Methods Heat Fluid Flow 33 (12) (2023) 4062–4089, http://dx.doi.org/10.1108/HFF-06-2023-0331.

[60] L. Chai, R. Shaukat, L. Wang, H.S. Wang, A review on heat transfer and hydrodynamic characteristics of nano/microencapsulated phase change slurry (N/MPCS) in mini/microchannel heat sinks, Appl. Therm. Eng. 135 (2018) 334–349, http://dx.doi.org/10.1016/j.applthermaleng.2018.02.068, URL: https://www.sciencedirect.com/science/article/pii/S1359431117354923.

[61] Z. Qiu, L. Li, Experimental and numerical investigation of laminar heat transfer of microencapsulated phase change material slurry (MPCMS) in a circular tube with constant heat flux, Sustain. Cities Soc. 52 (2020) 101786, http://dx.doi.org/10.1016/j.scs.2019.101786, URL: https://www.sciencedirect.com/science/article/pii/S2210670719316269.

[62] B. Chen, X. Wang, R. Zeng, Y. Zhang, X. Wang, J. Niu, Y. Li, H. Di, An experimental study of convective heat transfer with microencapsulated phase change material suspension: Laminar flow in a circular tube under constant heat flux, Exp. Therm. Fluid Sci. 32 (8) (2008) 1638–1646, http://dx.doi.org/10.1016/j.expthermflusci.2008.05.008, URL: https://www.sciencedirect.com/science/article/pii/S0894177708000708.

[63] S.M.H. Zadeh, S. Mehryan, M. Sheremet, M. Ghodrat, M. Ghalambaz, Thermo-hydrodynamic and entropy generation analysis of a dilute aqueous suspension enhanced with nano-encapsulated phase change material, Int. J. Mech. Sci. 178 (2020) 105609, http://dx.doi.org/10.1016/j.ijmecsci.2020.105609, URL: https://www.sciencedirect.com/science/article/pii/S0020740320305610.

[64] X. Wang, R.H. Rasheed, B. Keivani, D.J. Jasim, A.J. Sultan, S. Hamedi, H. Kazemi-Varnamkhasti, S. Salahshour, D. Toghraie, Thermal performance of forced convection of water- NEPCM nanofluid over a semi-cylinder heat source, Case Stud. Therm. Eng. 55 (2024) 104149, http://dx.doi.org/10.1016/j.csite.2024.104149, URL: https://www.sciencedirect.com/science/article/pii/S2214157X24001801.

[65] M. Hashemi-Tilehnoee, A. Dogonchi, S.M. Seyyedi, M. Sharifpur, Magneto-fluid dynamic and second law analysis in a hot porous cavity filled by nanofluid and nano-encapsulated phase change material suspension with different layout of cooling channels, J. Energy Storage 31 (2020) 101720, http://dx.doi.org/10.1016/j.est.2020.101720, URL: https://www.sciencedirect.com/science/article/pii/S2352152X20315577.

[66] Z. Qiu, L. Li, Experimental and numerical investigation of laminar heat transfer of microencapsulated phase change material slurry (MPCMS) in a circular tube with constant heat flux, Sustain. Cities Soc. 52 (2020) 101786, http://dx.doi.org/10.1016/j.scs.2019.101786, URL: https://www.sciencedirect.com/science/article/pii/S2210670719316269.

[67] K. Khanafer, K. Vafai, A critical synthesis of thermophysical characteristics of nanofluids, in: Nanotechnology and Energy, Jenny Stanford Publishing, 2017, pp. 279–332.

[68] A. Zaraki, M. Ghalambaz, A.J. Chamkha, M. Ghalambaz, D. De Rossi, Theoretical analysis of natural convection boundary layer heat and mass transfer of nanofluids: Effects of size, shape and type of nanoparticles, type of base fluid and working temperature, Adv. Powder Technol. 26 (3) (2015) 935–946, http://dx.doi.org/10.1016/j.apt.2015.03.012, URL: https://www.sciencedirect.com/science/article/pii/S0921883115000734. Special issue of the 7th World Congress on Particle Technology.

[69] S. Barlak, O.N. Sara, A. Karaipekli, S.Y. and, Thermal conductivity and viscosity of nanofluids having nanoencapsulated phase change material, Nanoscale Microscale Thermophys. Eng. 20 (2) (2016) 85–96, http://dx.doi.org/10.1080/15567265.2016.1174321.

[70] T. Khadiran, M.Z. Hussein, Z. Zainal, R. Rusli, Nano-encapsulated n-nonadecane using vinyl copolymer shell for thermal energy storage medium, Macromol. Res. 23 (2015) 658–669.

[71] E. Shchukina, M. Graham, Z. Zheng, D. Shchukin, Nanoencapsulation of phase change materials for advanced thermal energy storage systems, Chem. Soc. Rev. 47 (11) (2018) 4156–4175.

[72] J. Pereira, A. Moita, A. Moreira, An overview of the nano-enhanced phase change materials for energy harvesting and conversion, Molecules 28 (15) (2023) http://dx.doi.org/10.3390/molecules28155763, URL: https://www.mdpi.com/1420-3049/28/15/5763.

[73] O. Younis, A. Abderrahmane, M. Hatami, A. Mourad, K. Guedri, Nanoencapsulated phase change material in a trapezoidal prism wall under the magnetic field effect for energy storage purposes, Sci. Rep. 13 (1) (2023) 16060, http://dx.doi.org/10.1038/s41598-023-43394-2.

[74] C. Ho, Y.-C. Liu, M. Ghalambaz, W.-M. Yan, Forced convection heat transfer of Nano-Encapsulated Phase Change Material (NEPCM) suspension in a mini-channel heatsink, Int. J. Heat Mass Transfer 155 (2020) 119858, http://dx.doi.org/10.1016/j.ijheatmasstransfer.2020.119858, URL: https://www.sciencedirect.com/science/article/pii/S0017931020303641.

[75] Y. Zhang, H. Lin, R. Chaturvedi, P.K. Singh, I.B. Mansir, K. Zhang, J. Alhoee, Mixed convection of EG/NEPCM inside a lid-driven cavity with a rotating cylinder, Case Stud. Therm. Eng. 47 (2023) 103072, http://dx.doi.org/10.1016/j.csite.2023.103072, URL: https://www.sciencedirect.com/science/article/pii/S2214157X23003787.

[76] H.F. Öztop, H. Coşanay, N. Biswas, F. Selimefendigil, Analysis of natural convection and melting in a separated cavity with nano-enhanced phase change material filled wall, Arab. J. Sci. Eng. 49 (8) (2024) 10653–10668, http://dx.doi.org/10.1007/s13369-023-08463-8.

[77] M. Ghalambaz, M. Mozaffari, S. Yazdani, M. Abbaszadeh, M. Sheremet, M. Ghalambaz, Conjugate entropy generation and heat transfer of a dilute suspension of nano-encapsulated phase change material in a partially heated wall cavity, Rep. Mech. Eng. 4 (1) (2023) 175–192.

[78] M. Akbarzadeh, S. Rashidi, N. Karimi, N. Omar, First and second laws of thermodynamics analysis of nanofluid flow inside a heat exchanger duct with wavy walls and a porous insert, J. Therm. Anal. Calorim. 135 (1) (2019) 177–194, http://dx.doi.org/10.1007/s10973-018-7044-y.

[79] M. Jahanshahi, S. Hosseinizadeh, M. Alipanah, A. Dehghani, G. Vakilinejad, Numerical simulation of free convection based on experimental measured conductivity in a square cavity using water/SiO2 nanofluid, Int. Commun. Heat Mass Transfer 37 (6) (2010) 687–694, http://dx.doi.org/10.1016/j.icheatmasstransfer.2010.03.010, URL: https://www.sciencedirect.com/science/article/pii/S0735193310000722.

[80] Y.M. Seo, K. Luo, M.Y. Ha, Y.G. Park, Direct numerical simulation and artificial neural network modeling of heat transfer characteristics on natural convection with a sinusoidal cylinder in a long rectangular enclosure, Int. J. Heat Mass Transfer 152 (2020) 119564, http://dx.doi.org/10.1016/j.ijheatmasstransfer.2020.119564, URL: https://www.sciencedirect.com/science/article/pii/S001793101935481X.